Research Article

Faisal Shahzad, Wasim Jamshed*, Rabia Safdar*, Syed M. Hussain, Nor Ain Azeany Mohd Nasir, Mallinath Dhange, Kottakkaran Sooppy Nisar, Mohamed R. Eid, Muhammad Sohail, Mishal Alsehli, and Ashraf Elfasakhany

Thermal analysis characterisation of solar-powered ship using Oldroyd hybrid nanofluids in parabolic trough solar collector: An optimal thermal application

https://doi.org/10.1515/ntrev-2022-0108
received November 17, 2021; accepted March 26, 2022

Abstract: The mathematical modeling of hybrid nanofluid flow and heat transfer with entropy generation toward parabolic trough surface collector (PTSC) inside the solar-powered ship (SPS) is performed. The mathematical model used non-Newtonian Oldroyd-B model amidst a constant inclined magnetic field influence is being considered. The mathematical model is then reduced by adopting appropriate similarity transformation into a higher-order nonlinear differential equations system. The reduced model is computed using the well-known technique called the Keller Box scheme. Physical parameters effectiveness, for instance, thermal radiation, viscous dissipation, hybrid nanoparticles, and Joule heating, is displayed in graphs. The silver-ethylene glycol (Ag-EG) characteristic performance outperformed the silver-magnetite-ethylene glycol (Ag-Fe_3O_4/EG). The maximum efficiency of Ag-EG is about 26.3%, while the minimum is at least 5.6%.

Keywords: PTSC, solar-powered ship, angle of inclination, Oldroyd B-hybrid nanofluid, entropy formation, MHD, Keller box method

*** Corresponding author: Wasim Jamshed,** Department of Mathematics, Capital University of Science and Technology (CUST), Islamabad, 44000, Pakistan, e-mail: wasiktk@hotmail.com
*** Corresponding author: Rabia Safdar,** Department of Mathematics, Lahore College for Women University, 54000, Lahore, Pakistan, e-mail: rabia.safdar1109@gmail.com
Faisal Shahzad: Department of Mathematics, Capital University of Science and Technology (CUST), Islamabad, 44000, Pakistan
Syed M. Hussain: Department of Mathematics, Faculty of Science, Islamic University of Madinah, Madinah, 42351, Saudi Arabia
Nor Ain Azeany Mohd Nasir: Department of Mathematics, Centre for Defence Foundation Studies, Universiti Pertahanan Nasional Malaysia, Kem Sungai Besi 57000, Kuala Lumpur, Malaysia
Mallinath Dhange: Department of Mathematics (Mathematics Research Center, Affiliated to Visvesvaraya Technological University Belagavi), BLDA's VP Dr PG Halakatti College of Engineering and Technology, Vijayapur, India
Kottakkaran Sooppy Nisar: Department of Mathematics, College of Arts and Sciences, Wadi Aldawaser, Prince Sattam bin Abdulaziz University, 11991, Saudi Arabia
Mohamed R. Eid: Department of Mathematics, Faculty of Science, New Valley University, Al-Kharga, Al-Wadi Al-Gadid, 72511, Egypt; Department of Mathematics, Faculty of Science, Northern Border University, Arar, 1321, Saudi Arabia
Muhammad Sohail: Department of Mathematics, Khwaja Fareed University of Engineering & Information Technology, Rahim Yar Khan 64200, Pakistan
Mishal Alsehli, Ashraf Elfasakhany: Mechanical Engineering Department, College of Engineering, Taif University, P.O. Box 11099, Taif 21944, Saudi Arabia

Nomenclature

b	initial stretching rate
B_γ	Biot number
B_r	Brinkman number
C_p	specific heat (J kg^{-1} K^{-1})
E_c	Eckert number
E_G	dimensional entropy (J/K)
h_f	heat transfer coefficient
κ	thermal conductivity (Wm^{-1} K^{-1})
k^*	absorption coefficient
N_q	radiation parameter
N_G	entropy generation (dimensionless)
Nu_x	local Nusselt number
Pr	Prandtl number (ν/α)
q_r	radiative heat flux
q_w	wall heat flux
R_e	Reynolds number
S	suction/injection parameter

u_1, u_2	velocity component (m s^{-1})
U_w	velocity of the stretching sheet
V_w	vertical velocity
x, y	dimensional space coordinates (m)

Greek symbols

Θ	fluid temperature
Θ_w	fluid temperature of the surface
Θ_∞	ambient temperature
ϕ,	solid volume fraction
ρ	density kg m^{-3}
$\sigma^\star$	Stefan Boltzmann constant
Γ_q	inclination angle
Λ_q	velocity slip parameter
μ	dynamic viscosity of the fluid (kg m^{-1} s^{-1})
ν	kinematic viscosity of the fluid (m^2 s^{-1})
Ω	temperature gradient (dimensionless)
$\xi^\star$	independent similarity variable
θ	temperature (dimensionless)
ψ	stream function

Subscripts

f	base fluid
p_1, p_2	nanoparticles
nf	nanofluid
hnf	hybrid nanofluid
s	particles
Ag	silver nanoparticles
Fe_3O_4	magnetite particles

1 Introduction

Solar radiation can accomplish heat by chemical processes or generate electricity, which is known as solar energy. The huge amount of solar energy that strikes earth satisfies the world's current and proposed energy needs by an extensive limit. This highly assigned source can fulfill all future energy demands if perfectly exploited. Solar energy is well known as a refined form of substitute energy. Increased energy has demand on the one side and the negative environmental encounter of fossil fuels on another side. Different countries deal with alternative energy origins to be a desired and practical choice for industrial and domestic use. The devaluation of organic contaminants in air and water streams regarded as one of the so-called advanced oxidation processes is one of the most important uses of this technology. To achieve the regulated absorption, reflection, or transmission of the appropriate wavelength of the solar spectrum, natural species have created intricate photonic nanostructures on numerous scales and dimensions in a hierarchical, structured manner. A bio-inspired strategy for solar energy manipulation is a powerful and promising method [1–3]. Energy is the most expensive component in the manufacturing of agricultural greenhouse crops in thermal climates. In addition, the upfront costs of fossil fuels and ordinary energy are rapidly rising. Solar energy has generated global interest because of the increasing consumption of finite fossil fuel supply as well as their impact on the environment. Many people at all levels of the society are unaware of the importance of solar energy [4,5]. An upgraded approximation of the interplanetary solar spectrum from 0 to 1,000 μm is recommended depending on the solar constant value. It is made by the division of the spectrum into nine bands and choosing typical (and latest) spectra for each band, as well as scaling coefficients that are appropriate [6].

Solar-powered ships are the energy generators that use the cleanest and renewable energy from the sun and convert it into thermal or electrical energy sources. There are many ways to capture solar energy. Usually, to transform solar power for domestic use, solar panel of photovoltaic systems is used. Raphael Domjan is the first person to initiate and complete the round-the-world trip with the help of solar energy within the duration of 2010–2012. He made polar solar navigation first in the Arctic Ocean in 2015. Solar Stratos was the first project created by him in the stratosphere. He has also made solar-free fall and jumped off from a solar plane first time in 2020. The planet Solar MS TURANOR was the first to use solar energy to go around the world on May 4, 2012, from Monaco in the West direction. Its engines can be charged with solar energy, and it can move non-stop for up to 72 h. Ahmed *et al.* [7] used nanofluids to study the cooling processes of photovoltaic thermal along with the concentrated photovoltaic thermal and other systems utilising solar energy. Khanafer and Vafai [8] presented an analysis on current advancements in nanofluids in the field of solar stills and collectors, along with storage systems of photovoltaic and thermal energy. By using different concentrations of the nanofluids, Lee *et al.* [9] studied working fluid to improve its capability in solar thermal systems. They analyzed the characteristics of nanofluids like heat transfer, electronic conductivity, and absorbance of UV rays. Olia *et al.* [10] used nanofluids as working fluids to check the impacts of various factors, including nanoparticles size and volumetric fraction along with working fluid type, on the behaviour of parabolic trough collectors. Vijayan and Rajasekaran [11] used a generation tank of hot water to examine the performance of nanofluids consisting of deionised water and aluminum oxide in the PTSC system used as thermal transfer fluids. Wole-Osho *et al.* [12] investigated the effect of various nanoparticles to determine the efficiency of solar collectors. Jamshed *et al.* [13] investigated the entropy production of non-Newtonian Maxwell single-walled and multi-walled carbon nanotube-engine oil nanofluids flowing in PTSC as an operating fluid inside SPS in the existence of Darcy–Forchheimer and Cattaneo–Christov models. They reached to multi-walled carbon nanotubes more efficacy of thermal exchange than single-walled carbon nanotubes. Bayones *et al.* [14] analyzed the solution by applying the finite element method on MoS_2-Cu/sodium alginate hybrid nanofluid flowing in PTSC at SPS implementation with the suction (injection) and slippery velocity. They concluded that the permeability reduces the heat transfer and boosts the frictional force.

Hybrid nanofluid is a type of nanofluid that is a good conductor of heat transfer compared to conventional fluids [15]. The composition of hybrid nanoparticles is useful for preparing these fluids. Due to enhanced thermal characteristics, these fluids are generally used in solar energy, ventilation, heat pipes, manufacturing, electronic cooling, automotive industry, and air conditioning applications [16]. Time-independent flow and thermal conductivity of the hybrid nanofluid passing through a stretchable have been studied by ref. [17]. To determine the boundary value, a problem solver (bvp4c) with Matlab software has been employed. Huang *et al.* [18] experimentally analyzed various impacts of a hybrid nanofluid mixture, including thermal conductivity and fall in pressure consisting of alumina nanoparticles and multiwalled carbon nanotubes (MWCNTs) in a chevron corrugated plate heat exchanger. It has been found in this study that the fall of temperature is less than Al_2O_3/water nanofluid and greater than water.

Acharya [19] proposed flow models with heat transfer features for hybrid nanofluids having an impact on nonlinear solar radiation for special solar thermal equipment. The hybrid solution reveals magnificent augmentation in heat transport for suction. The effects are being reduced by imposing the injections; a reduction in the spoil rate is observed for hybrid nanocomposite. Kumar *et al.* [20] proposed an analysis that involves the stability of heat transfer increment because of the impact of variation in valuable characteristics of fluids with thermal radiation ability along with the suspended hybrid nanofluids. The transfer of heat and properties of hybrid nanofluids in three dimensions under the constraint of turbulent through a parabolic trough solar collector (PTC) receiver was proposed [21]. The study of hybrid nanofluid used in solar energy absorption and tries to stoke the thermal energy was presented by ref. [22]. Recent additions considering fluids flow with heat and mass transfer in various physical situations are given by refs. [23–35].

Oldroyd-B fluid is a particular non-Newtonian fluid whose transfer behaviour could not be accurately described as the general relationship between share rate and shear pressure in the actual shear flow. Recently, numerous researchers have considered the various issues related to this fluid. The stable 3-D Oldroyd-B nanofluid flow on a two-way stretch surface evaluated the effects of heat production. Applicable similarity conversions are utilised for the minimisation of governing fractional differential equations by combining nonlinear general differential equations [36]. Properties of an Oldroyd-B nanofluid due to axis uniform rotating disk are examined by using the characteristics of the vertically appropriate magnetic field. The movement of fluid on the disk's surface is caused by turning along with the radically stretching of the disk [37,38]. The unsteady boundary surface flow and heat transfer of the incompressible Oldroyd-B nanofluid thin layer have been analyzed through the stretching sheet. The temperature and the velocity of the stretching sheet vary with sheet and time [39]. The association instability onset in a compact medium layer that is saturated with Oldroyd-B viscoelastic nanofluid has been examined by integrating the results of Brownian dispersion and thermophoresis. As a result, the eigenvalue problems are determined numerically with the help of the Galerkin method [40].

Many utilisations of non-Newtonian nanofluids in solar energy, industry, and engineering have led us to develop a complete model for the unstable 3D flow of the Oldroyd-B nanoparticles [41]. Three distinct partial models of the Oldroyd-B fluid are examined. The triple fractional analysis is presented to evaluate the resultant three models established by three partial operators [42]. Mathematical symmetry between the coaxial cylinders of the 1D partial Oldroyd-B nanofluid flow has been found for heat transfer with no pressure gradient [43].

A modern illustration of the postulate and utilisations of the numerous entropy enhancement fundamentals are specified. These principles involve Jaynes' maximum entropy principle (MaxEnt), generalised maximum entropy, Kullback's minimum cross-entropy principle (MinxEnt), minimum cross-entropy principles, minimum interdependence principle, inverse entropy optimisation principles, mini-max entropy principle, and definitely, dual entropy upsurge principles. The relationship between thermodynamic entropy and information-theoretic entropy is uniquely recollected in the background of more ordinary relations that managed among what are originated as essential and trivial entropies. References [44–53] have more detailed information.

Hybrid nanofluids show various benefits in contrast with the traditional forms by their reformed effects. A summary of solar energy systems is displayed, and then, the utilisation of hybrid nanofluids in numerous solar technologies, mainly solar thermal, is presented. Relation between nanofluid structure and traditional structure is presented to attain a complete understanding of the improvement of nanofluids. It follows from the previous discussion that the most important way to maximize the utilization of solar energy is to enhance the thermal properties of the convective fluid. Hybrid nanofluids, the expulsion of nanoparticle or nanocomposite brighten compound designs in conventional fluids, direct the investigation of the research in the current years due to the potential interdependent effects between particles. However, there are only few studies on efficient experimental analysis. The significant flaw of typical solar depends on its deficient production. In this study, enhancement of still solar performance using two-hybrid nanofluids is investigated. Using two conventional nanofluids and hot water was also exploited to discuss the development of solar energy. Hybrid nanofluids, conventional nanofluids, or hot water were connected to the solar system with heat conversation fixed at the base of the basin of the solar system [54–57]. Following that, plenty of other studies appears, each focusing on a different element of the problem [58–70], to name a few.

To select and evaluate the sufficient formation of solar curves, eight distinct models that are semi-theoretical are applied to the data of the experiment and compared with the help of determination coefficients that were forecasted by non-linear regression analysis by using the statistical computer program [71]. There is a tendency to describe the recent items immediately but not in the detained reconstruction. There is also a tendency to remember the first temporarily isolated objects. There is a priority for the forward recall order along with output order preferences, which minimize the path length during retrieval [72]. As a result of increasing the demand for global energy and increasing the short supply of conventional or produced crude oils by easy way, the most incredible attention is being rewarded to the exploitation of extra-heavy and unconventional heavy oils [73]. The thermophysical characteristics of nanofluids are necessary to forecast the behaviour of heat transfer. Numerical results, which are based on three oxide nanofluids and their hybrids, have been suggested. All the thermophysical effects of nanofluids are increasing with the inclusion of nanoparticles, and these effects also increase the thermal conductivity by more than 12%. By using theoretical results, the variability in viscosity evaluation and significant experimental correlations were found [74]. The advantages of using solar-powered ships/boats are eco-friendly, worth investing in, prevents noise pollution, long-time charging, replaces the dead boat battery, charging your devices, comparatively less environmental effect, extremely reliable, and connected on more than one level (Figure 1).

This study examines the heat transfer analysis of the solar water pump using mono/hybrid nanofluids (*i.e.*, Ag-EO and Ag-Fe_3O_4/EG) preceding a parabolic trough solar collector (PTSC) positioned innards a solar-powered ship. Considerations have been made on solar radiation as a heat source. Performance of thermal transfer of ship is analyzed for a circumstance of diverse influences such as thermal radiative flowing, viscous dissipation, and heat source. Entropy production scrutiny has been carried out in the case of Oldroyd-B hybrid nanofluid. The modeled equations in terms of momentum and energy have been handled using an entrenched numerical method, namely, the Keller box method (KBM). The effects of various diverse parameters about shear stress, velocity, temperature profiles, and coefficient of surface drag, including Nusselt number, are deliberated briefly as well as displayed in terms of figures and tables.

2 Present theoretical experiment

Efficiency of a solar-powered ship can be enhanced with the help of hybrid nanofluid flow on PTSC, and a theoretical experiment has been proposed. Various parts of SPS contain PTSC on them. The aim of the present analysis is presented in this section. PVC cell surfaces are replaced with PTSC in the presented model. PTSC equipment is cylindrical rather than absolute PVC surfaces. So more solar energy is absorbed on PTSC because of its huge surface area. Solar energy is cost-effective, and hence, solar-powered ships can be manufactured and maintained on a low budget. The continuous increase in oil prices it leads researchers to use solar energy, especially in the sea ship industry. According to the analysis, amplification in heat transfer and energy is obtained when hybrid nano-solid particles are combined into fluid flow on PTSC under the effects of viscous dissipation, thermal radiation, and thermal conduction. No pollution is

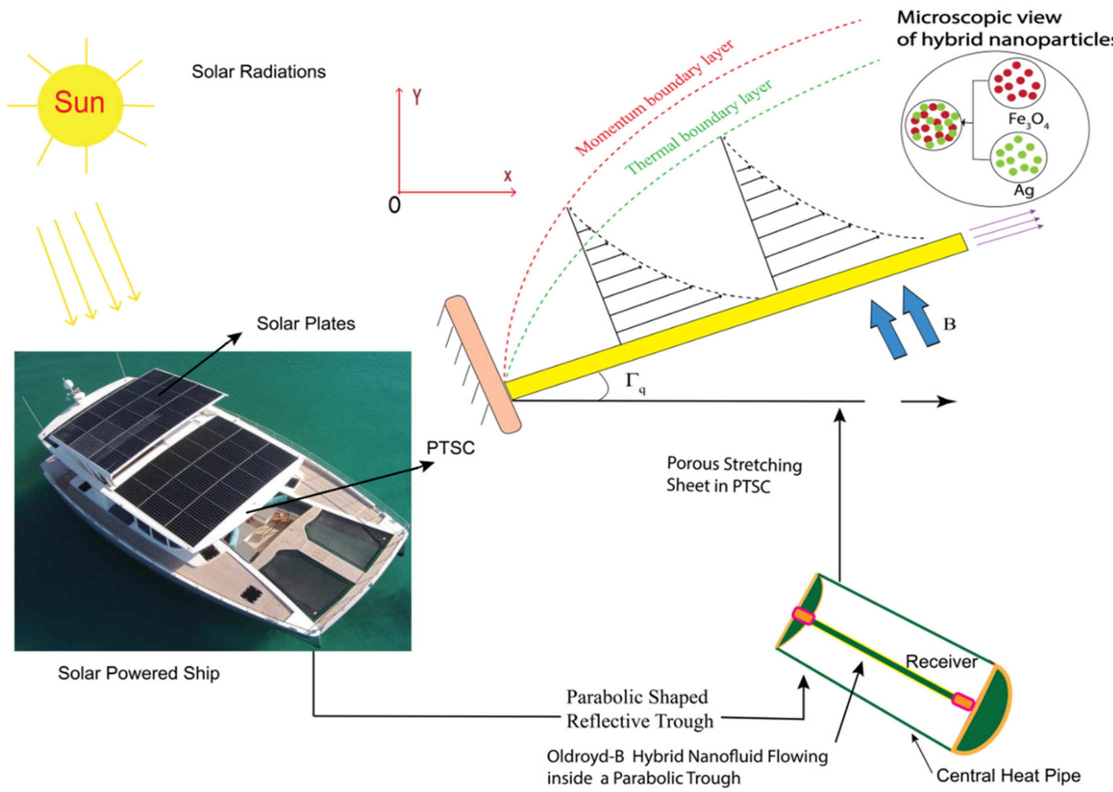

Figure 1: Parabolic trough solar collector.

created in an atmosphere with solar aircraft, as they are environment friendly.

3 Mathematical formulation

A mathematical model represents the moving flat horizontal surface (Figure 1) having a non-uniform stretching velocity:

$$U_w(x, 0) = bx. \tag{1}$$

3.1 Model equations

Constitutive flow equations on viscous Oldroyd-B hybrid nanofluid with common boundary layer estimations under the influence of inclined MHD, viscous dissipation, inclined Joule heating, and radiation heat flux are presented (see, for instance, ref. [75]):

$$\frac{\partial u_1}{\partial x} + \frac{\partial u_2}{\partial y} = 0, \tag{2}$$

$$\begin{aligned} u_1\frac{\partial u_1}{\partial x} + u_2\frac{\partial u_1}{\partial y} + \varrho_1\left[u_1^2\frac{\partial^2 u_1}{\partial x^2} + u_2^2\frac{\partial^2 u_1}{\partial y^2} + 2u_1u_2\frac{\partial^2 u_1}{\partial x\partial y}\right] \\ = \frac{\mu_{hnf}}{\rho_{hnf}}\left[\left(\frac{\partial^2 u_1}{\partial y^2}\right)\right] - \frac{\sigma_{hnf}B^2u_1}{\rho_{hnf}}\sin^2(\Gamma_q) \\ + \frac{\mu_{hnf}}{\rho_{hnf}}\left[\varrho_2\left(u_1\left(\frac{\partial^3 u_1}{\partial x\partial y^2}\right) - \frac{\partial u_1}{\partial x}\left(\frac{\partial^2 u_1}{\partial y^2}\right)\right.\right. \\ \left.\left. + \frac{\partial u_1}{\partial y}\left(\frac{\partial^2 u_2}{\partial y^2}\right) + u_2\left(\frac{\partial^3 u_1}{\partial y^3}\right)\right)\right], \end{aligned} \tag{3}$$

$$\begin{aligned} u_1\frac{\partial \Theta}{\partial x} + u_2\frac{\partial \Theta}{\partial y} = \frac{k_{hnf}}{(\rho C_p)_{hnf}}\left(\frac{\partial^2 \Theta}{\partial y^2}\right) - \frac{1}{(\rho C_p)_{hnf}}\left(\frac{\partial q_r}{\partial y}\right) \\ + \frac{\mu_{hnf}}{(\rho C_p)_{hnf}}\left(\frac{\partial u_1}{\partial y}\right)^2 + \frac{\sigma_{hnf}B^2u_1^2}{(\rho C_p)_{hnf}}\sin^2(\Gamma_q). \end{aligned} \tag{5}$$

Aziz *et al.* [76] provided boundary conditions:

$$\begin{aligned} u_1(x, 0) = U_w + N_L\left(\frac{\partial u}{\partial y}\right), \quad u_2(x, 0) = V_w, \\ -k_0\left(\frac{\partial \Theta}{\partial y}\right) = h_f(\Theta_w - \Theta), \end{aligned} \tag{6}$$

$$u_1 \to 0, \quad \frac{\partial u_1}{\partial y} \to 0, \ \Theta \to \Theta_\infty \quad \text{as } y \to \infty. \tag{7}$$

Table 1: Thermophysical properties of Oldroyd-B nanofluid

Properties	Nanofluid
Dynamic viscosity (μ)	$\mu_{nf} = \mu_f(1-\phi)^{-2.5}$
Density (ρ)	$\rho_{nf} = (1-\phi)\rho_f + \phi\rho_s$
Heat capacity (ρC_p)	$(\rho C_p)_{nf} = (1-\phi)(\rho C_p)_f + \phi(\rho C_p)_s$
Thermal conductivity (κ)	$\frac{\kappa_{nf}}{\kappa_f} = \left[\frac{(\kappa_s + (2)\kappa_f) - (2)\phi(\kappa_f - \kappa_s)}{(\kappa_s + (2)\kappa_f) + \phi(\kappa_f - \kappa_s)}\right]$
Electrical conductivity (σ)	$\frac{\sigma_{nf}}{\sigma_f} = \left[1 + \frac{3\left(\frac{\sigma_s}{\sigma_f} - 1\right)\phi}{\left(\frac{\sigma_s}{\sigma_f} + 2\right) - \left(\frac{\sigma_s}{\sigma_f} - 1\right)\phi}\right]$

Here, $\overleftarrow{V} = [u_1(x, y, 0), u_2(x, y, 0), 0]$ is a vector regarding flow velocity. Θ is the signifying fluid temperature. The penetrability of the expanding plate is signified by V_w, slip length, heat transfer coefficient N_L, and h_f and k_0 represent the porousness of material. Convectional heated surface underwent its thermal loss due to conduction (Newtonian heating), and the flow velocity near the surface is proportional to the shear stress exerts in it (slip condition).

3.2 Thermophysical properties regarding Oldroyd-B nanofluid

When nanoparticles are dispersed in ethylene glycol fluid, the thermophysical property is enhanced. A summary about physical parameters for Oldroyd-B nanofluid is provided in Table 1 [77–80].

ϕ has represented the coefficient of nanoparticle volumetric fraction. μ_f, ρ_f, $(C_p)_f$, κ_f, and σ_f are, respectively, dynamic viscosity, density, effective heat capacity, the thermal conductivity, and electrical conductivity of the base fluid. Other parameters including ρ_s, $(C_p)_s$, κ_s, and σ_s are, respectively, density, adequate heat capacity, thermal conductivity, and electral conductivity of nanoparticles.

3.3 Thermophysical characteristics of the Oldroyd-B hybrid nanofluid

Hybrid nanofluids work when there is a suspension of two different nanoparticle types in the working fluid. Suspension increases the heat transfer ability of ordinary fluids meanwhile proving them better heat boosters than nanofluids. Physical factors of Oldroyd-B hybrid nanofluid are summarised in Table 2 [81–83].

In Table 2, μ_{hnf}, ρ_{hnf}, $\rho(C_p)_{hnf}$, κ_{hnf}, and σ_{hnf} are dynamics viscosity, density, specific heat capacity, and the thermal and electrical conductivity of hybrid nanofluid, respectively. ϕ and $\phi_{hnf} = \phi_R + \phi_H$ are coefficients of nanoparticle volume concentration for ordinary nanofluid and hybrid nanofluid, respectively. μ_f, ρ_f, $(C_p)_f$, κ_f, and σ_f are dynamic viscosity, intensity, specific heat capacity, and the thermal and electrical conductivity of working fluid, respectively. ρ_{p_1}, ρ_{p_2}, $(C_p)_{p_1}$, $(C_p)_{p_2}$, κ_{p_1}, κ_{p_2}, σ_{p_1}, and σ_{p_2} are parameters of density, specific heat capacity, thermal conductance, and electrical conductance of nanoparticles.

3.4 Nanoparticles and base fluid features

Physical properties of ethylene glycol (working fluid), as well as other used nanoparticles in the current analysis, are described in Table 3 [84–86],

Table 2: Thermophysical characteristics of Oldroyd-B hybrid nanofluids

Features	Hybrid nanofluid
Viscosity (μ)	$\mu_{hnf} = \mu_f(1-\phi_R)^{-2.5}(1-\phi_H)^{-2.5}$
Density (ρ)	$\rho_{hnf}=[(1-\phi_H)\{(1-\phi_R)\rho_f + \phi_R\rho_{p_1}\}]+\phi_H\rho_{p_2}$
Heat capacity (ρC_p)	$(\rho C_p)_{hnf} = [(1-\phi_H)\{(1-\phi_R)(\rho C_p)_f + \phi_R(\rho C_p)_{p_1}\}] + \phi_H(\rho C_p)_{p_2}$
Thermal conductivity (κ)	$\frac{\kappa_{hnf}}{\kappa_{gf}} = \left[\frac{(\kappa_{p2} + \kappa_{gf}) - \phi_H(\kappa_{gf} - \kappa_{p2})}{(\kappa_{p2} + \kappa_{gf}) + \phi_H(\kappa_{gf} - \kappa_{p2})}\right]$; $\frac{\kappa_{gf}}{\kappa_f} = \left[\frac{(\kappa_{p1} + \kappa_f) - \phi_R(\kappa_f - \kappa_{p1})}{(\kappa_{p1} + \kappa_f) + \phi_R(\kappa_f - \kappa_{p1})}\right]$
Electrical conductivity (σ)	$\frac{\sigma_{hnf}}{\sigma_f} = \left[1 + \frac{3\left(\frac{\phi_R\sigma_{p1} + \phi_H\sigma_{p2}}{\sigma_f} - (\phi_R + \phi_H)\right)}{\left(\frac{\phi_R\sigma_{p1} + \phi_2\sigma_{p2}}{(\phi_R + \phi_H)\sigma_f} + 2\right) - \left(\frac{\phi_R\sigma_{p1} + \phi_H\sigma_{p2}}{\sigma_f} - (\phi_R + \phi_H)\right)}\right]$

Table 3: Physical features of base fluid as well as nanoparticles at 293 K

Thermophysical	ρ (kgm^{-3})	c_p (JkgK^{-1})	k (WmK^{-1})	σ (Sm^{-1})
Ethylene glycol (EG)	1114	2415	0.252	5.5×10^{-6}
Magnetite (Fe_3O_4)	5180	670	9.7	25.000
Silver (Ag)	10500	235	429	6.3×10^7

3.5 Rosseland approximations

Roseland approximation [87] can be written as follows:

$$q_r = -\frac{4\sigma^\star}{3k^\star}\frac{\partial\Theta^4}{\partial y}, \tag{8}$$

where $\sigma^\star$ and $k^\star$ are Stefan Boltzmann number and absorption coefficient, respectively.

4 The solution for the problem

Equations of boundary value problem (2)–(5) are converted *via* similarity technique that changes governing PDEs in ODEs. Stream functions ψ are introduced as follows:

$$u_1 = \frac{\partial\psi}{\partial y}, u_2 = -\frac{\partial\psi}{\partial x}, \tag{9}$$

with similarity variables [77].

$$\xi^\star(x,y) = \sqrt{\frac{b}{\nu_f}}y,\ \psi(x,y) = \sqrt{\nu_f b}\,xf(\xi^\star),\quad \theta(\xi^\star) = \frac{\Theta - \Theta_\infty}{\Theta_w - \Theta_\infty}, \tag{10}$$

in governing equations (2)–(5). The following relation is obtained:

$$f''' + \phi_a\phi_b[ff'' - f'^2 + \chi_1(2ff' - f^2f''')] + \chi_2(f''^2 - ff^{iv}) - \frac{\phi_d}{\phi_b}M\sin^2(\Gamma_q)f' = 0, \tag{11}$$

$$\theta''\left(1 + \frac{1}{\phi_e}\mathrm{Pr}N_q\right) + \mathrm{Pr}\frac{\phi_c}{\phi_e}\left[f\theta' - f'\theta + \frac{E_c}{\phi_a\phi_c}f''^2 + \frac{\phi_d}{\phi_c}ME_c\sin^2(\Gamma_q)f'^2\right] = 0, \tag{12}$$

with

$$\left.\begin{matrix} f(0) = S,\ f'(0) = 1 + \Lambda_q f''(0),\ \theta'(0) = -B_\gamma(1 - \theta(0)) \\ f'(\xi^\star) \to 0,\ f''(\xi^\star) \to 0,\ \theta(\xi^\star) \to 0,\ \text{as } \xi^\star \to \infty \end{matrix}\right\}, \tag{13}$$

where $\phi'_i s$ with $a \le i \le e$ in equations (11–12) represent thermophysical properties about Oldroyd-B nanofluid as mentioned earlier:

$$\phi_a = (1 - \phi_R)^{2.5}(1 - \phi_H)^{2.5},\quad \phi_b = (1 - \phi_H)\left\{(1 - \phi_R) + \phi_R\frac{\rho_{p_1}}{\rho_f}\right\} + \phi_H\frac{\rho_{p_2}}{\rho_f}, \tag{14}$$

$$\phi_c = (1 - \phi_H)\left\{(1 - \phi_R) + \phi_R\frac{(\rho C_p)_{p_1}}{(\rho C_p)_f}\right\} + \phi_H\frac{(\rho C_p)_{p_2}}{(\rho C_p)_f}, \tag{15}$$

$$\phi_d = \frac{\sigma_{hnf}}{\sigma_f} = \left[1 + \frac{3\left(\frac{\phi_R\sigma_{p_1} + \phi_H\sigma_{p_2}}{\sigma_f} - (\phi_R + \phi_H)\right)}{\left(\frac{\phi_R\sigma_{p_1} + \phi_2\sigma_{p_2}}{(\phi_R + \phi_H)\sigma_f} + 2\right) - \left(\frac{\phi_R\sigma_{p_1} + \phi_H\sigma_{p_2}}{\sigma_f} - (\phi_R + \phi_H)\right)}\right], \tag{16}$$

$$\phi_e = \left[\frac{(\kappa_{p_2} + \kappa_{gf}) - \phi_H(\kappa_{gf} - \kappa_{p_2})}{(\kappa_{p_2} + \kappa_{gf}) + \phi_H(\kappa_{gf} - \kappa_{p_2})}\right]\left[\frac{(\kappa_{p_1} + \kappa_f) + \phi_R(\kappa_f - \kappa_{p_1})}{(\kappa_{p_1} + \kappa_f) - \phi_R(\kappa_f - \kappa_{p_1})}\right]. \tag{17}$$

As equation (2) satisfied identically, the notation ($'$) is expressing derivatives according to $\Psi^\star$. Here, $\chi_1 = b\varrho_1$ (Deborah number-I), $\chi_1 = b\varrho_2$ (Deborah number-II) defined along with $M = \frac{\sigma_f B_o^2}{c\rho_f}$ (magnetic field) parameter, $\mathrm{Pr} = \frac{\nu_f}{\alpha_f}$ (Prandtl number), $\alpha_f = \frac{\kappa_f}{(\rho C_p)_f}$ (thermal diffusivity), $S = -V_w\sqrt{\frac{1}{\nu_f b}}$ (mass transfer), $N_q = \frac{16}{3}\frac{\sigma^\star\Theta_\infty^3}{\kappa^\star\nu_f(\rho C_p)_f}$ (thermal radiation), $E_c = \frac{U_w^2}{(C_p)_f(\Theta_w - \Theta_\infty)}$ (Eckert number) $\Lambda_q = \sqrt{\frac{b}{\nu_f}}N_L$ (velocity slip), and $B_\gamma = \frac{h_f}{k_0}\sqrt{\frac{\nu_f}{b}}$ (Biot number) parameters.

4.1 Nusselt number

The physical entity that glows governing is the local Nusselt number (Nu_x), stated as follows:

$$\mathrm{Nu}_x = \frac{xq_w}{k_f(\Theta_w - \Theta_\infty)}, \tag{18}$$

where q_w represents the heat flux that is determined with

$$q_w = -k_{hnf}\left(1 + \frac{16}{3}\frac{\sigma^*\Theta_\infty^3}{\kappa^*\nu_f(\rho C_p)_f}\right)\left(\frac{\partial\Theta}{\partial y}\right)_{y=0}. \tag{19}$$

The results of the application of non-dimensional transformations (10) are represented as follows:

$$\mathrm{Nu}_x\mathrm{Re}_x^{-\frac{1}{2}} = -\frac{k_{hnf}}{k_f}(1 + N_q)\theta'(0), \tag{20}$$

where Nu_x is the reduced Nusselt number. $\mathrm{Re}_x = \frac{U_w x}{\nu_f}$ is the local Re depending on the stretching velocity ($U_w(x)$).

4.2 Entropy generation analysis

Mentioned considerations have the following entropy production equation:

$$\begin{aligned} E_G = {} & \frac{k_{hnf}}{\Theta_\infty^2}\left\{\left(\frac{\partial\Theta}{\partial y}\right)^2 + \frac{16}{3}\frac{\sigma^*\Theta_\infty^3}{\kappa^*\nu_f(\rho C_p)_f}\left(\frac{\partial\Theta}{\partial y}\right)^2\right\} \\ & + \frac{\mu_{hnf}}{\Theta_\infty}\left(\frac{\partial u_1}{\partial y}\right)^2 + \frac{\sigma_{hnf}B^2\sin^2(\Gamma_q)u_1{}^2}{\Theta_\infty}. \end{aligned} \tag{21}$$

Entropy equation has the following dimensionless form:

$$N_G = \frac{\Theta_\infty{}^2 b^2 E_G}{k_f(\Theta_w - \Theta_\infty)^2}. \tag{22}$$

Dimensionless entropy equation obtained from equation (10) is expressed as follows:

$$\begin{aligned} N_G = \mathrm{Re}\Bigg[& \phi_e(1 + N_q)\theta'^2 + \frac{1}{\phi_a}\frac{B_r}{\Omega}(f''^2 \\ & + \phi_a\phi_d M\sin^2(\Gamma_q)f'^2)\Bigg]. \end{aligned} \tag{23}$$

5 Numerical implementation

Non-linear ordinary differential equations (9)–(11) are tackled along with endpoint condition (2.12) *via* implementation of Keller box scheme [88] and algebraic software Matlab for all involved parametric values. The Keller box process is presented as a step-by-step in the flow chart in Figure 2.

5.1 ODE conversion

Required substitutions about the conversion of higher-order ODEs in first-order ODEs are already introduced. Introduction regarding dependent variables Vk_1, Vk_2, Vk_3, Vk_4, Vk_5, and Vk_6 is as follows:

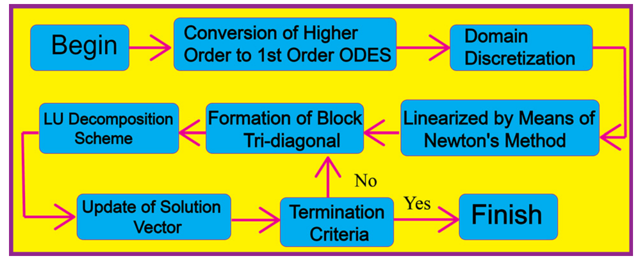

Figure 2: Flow chart of Keller box scheme.

$$\begin{gathered} Vk_1 = f,\ Vk_2 = f',\ Vk_3 = f'',\ Vk_4 = f''', \\ Vk_5 = \theta,\ Vk_6 = \theta'. \end{gathered} \tag{24}$$

$$\frac{\mathrm{d}Vk_1}{\mathrm{d}\xi^*} = Vk_2, \tag{25}$$

$$\frac{\mathrm{d}Vk_2}{\mathrm{d}\xi^*} = Vk_3, \tag{26}$$

$$\frac{\mathrm{d}Vk_3}{\mathrm{d}\xi^*} = Vk_4, \tag{27}$$

$$\frac{\mathrm{d}Vk_5}{\mathrm{d}\xi^*} = Vk_6, \tag{28}$$

$$\begin{aligned} & -\chi_2 Vk_1\frac{\mathrm{d}Vk_4}{\mathrm{d}\xi^*} + \chi_2 Vk_3^2 + \phi_a\phi_b Vk_1Vk_3 - \phi_a\phi_b Vk_2^2 \\ & + 2\phi_a\phi_b\chi_1 Vk_1Vk_2 - \phi_a\phi_b\chi_1 Vk_1^2Vk_4 \\ & - \frac{\phi_d}{\phi_b}M\sin^2(\Gamma_q)Vk_2 + Vk_4 = 0, \end{aligned} \tag{29}$$

$$\begin{aligned} & \frac{\mathrm{d}Vk_6}{\mathrm{d}\xi^*} + \frac{1}{\phi_d}\mathrm{Pr}\,N_q\frac{\mathrm{d}Vk_6}{\mathrm{d}\xi^*} + \mathrm{Pr}\frac{\phi_c}{\phi_d}Vk_1Vk_6 \\ & - \mathrm{Pr}\frac{\phi_c}{\phi_d}Vk_2Vk_5 + \mathrm{Pr}\frac{Ec}{\phi_a\phi_e}Vk_3^2 \\ & + \mathrm{Pr}\frac{\phi_d}{\phi_e}MEc\sin^2(\Gamma_q)Vk_2^2 = 0, \end{aligned} \tag{30}$$

$$\left.\begin{aligned} & Ov_1(0) = S,\ Ov_2(0) = 1 + \frac{\Lambda_q}{\phi_a}Vk_3(0), \\ & Vk_6(0) = -B_q(1 - Vk_5(0)), \\ & Vk_2(\xi^*) \to 0,\ Vk_3(\xi^*) \to 0,\ Vk_5(\xi^*) \to 0, \\ & \text{as } \xi^* \to \infty. \end{aligned}\right\} \tag{31}$$

5.2 Domain discretisation and difference equations

Following grid points are employed for divisions of the domain [0,1] with the help of regular mesh (Figure 3):

$$\xi_0^* = 0,\ \xi_j^* = \xi_{j-1}^* + \Delta x_j,\ j = 0, 1, 2, 3\ldots,J,\ \xi_J^* = 1,$$

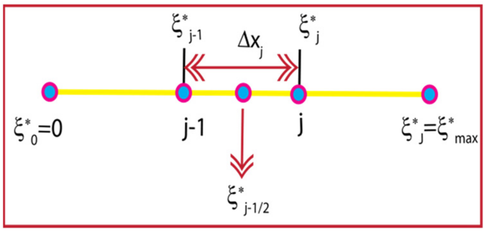

Figure 3: Typical grid structure for difference approximations.

where, Δx_j is step-size. First-order ODEs (17–24) are further solved with the central difference method at the midpoint $\xi^*_{j-1/2}$, and the following equations are obtained:

$$(Vk_1)_j - (Vk_1)_{j-1} = 0.5\Delta x_j((Vk_2)_j + (Vk_2)_{j-1}), \tag{32}$$

$$(Vk_2)_j - (Vk_2)_{j-1} = 0.5\Delta x_j((Vk_3)_j + (Vk_3)_{j-1}), \tag{33}$$

$$(Vk_3)_j - (Vk_3)_{j-1} = 0.5\Delta x_j((Vk_4)_j + (Vk_4)_{j-1}), \tag{34}$$

$$(Vk_5)_j - (Vk_5)_{j-1} = 0.5\Delta x_j((Vk_6)_j + (Vk_6)_{j-1}), \tag{35}$$

$$\left.\begin{aligned}&-\chi_2\frac{((Vk_1)_j + (Vk_1)_{j-1})}{2}((Vk_4)_j - (Vk_4)_{j-1})\\&\quad + \Delta x_j\chi_2\frac{((Vk_3)_j + (Vk_3)_{j-1})^2}{4}\\&+ \Delta x_j\phi_a\phi_b\frac{((Vk_1)_j + (Vk_1)_{j-1})}{2}\frac{((Vk_3)_j + (Vk_3)_{j-1})}{2}\\&\quad - \phi_a\phi_b\frac{((Vk_2)_j + (Vk_2)_{j-1})^2}{4}\\&+ 2\Delta x_j\phi_a\phi_b\chi_1\frac{((Vk_1)_j + (Vk_1)_{j-1})}{2}\frac{((Vk_2)_j + (Vk_2)_{j-1})}{2}\\&\quad - \Delta x_j\phi_a\phi_b\chi_1\frac{((Vk_1)_j + (Vk_1)_{j-1})^2}{4}\\&\times\frac{((Vk_4)_j + (Vk_4)_{j-1})}{2}\\&\quad - \Delta x_j\frac{\phi_d}{\phi_b}M\sin^2(\Gamma_q)\frac{((Vk_2)_j + (Vk_2)_{j-1})}{2}\\&+ \Delta x_j\frac{((Vk_4)_j + (Vk_4)_{j-1})}{2} = 0,\end{aligned}\right\}, \tag{36}$$

$$\left.\begin{aligned}&(Vk_6)_j - (Vk_6)_{j-1} + \frac{1}{\phi_d}\Pr N_q((Vk_6)_j - (Vk_6)_{j-1})\\&\quad + \Delta x_j\Pr\frac{\phi_c}{\phi_d}\frac{((Vk_1)_j + (Vk_1)_{j-1})}{2}\\&\times\frac{((Vk_6)_j + (Vk_6)_{j-1})}{2}\\&\quad - \Delta x_j\Pr\frac{\phi_c}{\phi_d}\frac{((Vk_2)_j + (Vk_2)_{j-1})}{2}\frac{((Vk_5)_j + (Vk_5)_{j-1})}{2}\\&+ \Pr\frac{Ec}{\phi_a\phi_e}\frac{((Vk_3)_j + (Vk_3)_{j-1})^2}{4}\\&\quad + \Pr\frac{\phi_d}{\phi_e}MEc\sin^2(\Gamma_q)\frac{((Vk_2)_j + (Vk_2)_{j-1})^2}{4} = 0,\end{aligned}\right\}. \tag{37}$$

5.3 Newton linearisation

Following substitutions about Newton's linearisation method are done on equations (34–39) for linearisation:

$$\left.\begin{aligned}(Vk_1)_j^{n+1} &= (Vk_1)_j^n + (\delta Ov_1)_j^n, (Vk_2)_j^{n+1}\\&= (Vk_2)_j^n + (\delta Ov_2)_j^n,\\(Vk_3)_j^{n+1} &= (Vk_3)_j^n + (\delta Vk_3)_j^n, (Vk_4)_j^{n+1}\\&= (Vk_4)_j^n + (\delta Vk_4)_j^n,\\(Vk_5)_j^{n+1} &= (Vk_5)_j^n + (\delta Vk_5)_j^n, (Vk_6)_j^{n+1}\\&= (Vk_6)_j^n + (\delta Vk_6)_j^n.\end{aligned}\right\} \tag{38}$$

Substituting equation (38) into equations (26–33) and ignoring square and higher powers of δ, the following equations are obtained:

$$\begin{aligned}&((\delta Ov_1)_j - (\delta Ov_1)_{j-1}) - 0.5\Delta x_j((\delta Ov_2)_j + (\delta Ov_2)_{j-1})\\&\quad = (r_1)_j,\end{aligned} \tag{39}$$

$$\begin{aligned}&((\delta Ov_2)_j - (\delta Ov_2)_{j-1}) - 0.5\Delta x_j((\delta Vk_3)_j + (\delta Vk_3)_{j-1})\\&\quad = (r_2)_j,\end{aligned} \tag{40}$$

$$\begin{aligned}&((\delta Vk_3)_j - (\delta Vk_3)_{j-1}) - 0.5\Delta x_j((\delta Vk_4)_j + (\delta Vk_4)_{j-1})\\&\quad = (r_3)_j,\end{aligned} \tag{41}$$

$$\begin{aligned}&((\delta Vk_5)_j - (\delta Vk_5)_{j-1}) - 0.5\Delta x_j((\delta Vk_6)_j + (\delta Vk_6)_{j-1})\\&\quad = (r_4)_j,\end{aligned} \tag{42}$$

$$\begin{aligned}&(\Upsilon_1)_j(\delta Ov_1)_j + (\Upsilon_2)_j(\delta Ov_1)_{j-1} + (\Upsilon_3)_j(\delta Ov_2)_j\\&\quad + (\Upsilon_4)_j(\delta Ov_2)_{j-1} + (\Upsilon_5)_j(\delta Vk_3)_j + (\Upsilon_6)_j(\delta Vk_3)_{j-1}\\&\quad + (\Upsilon_7)_j(\delta Vk_4)_j + (\Upsilon_8)_j(\delta Vk_4)_{j-1} = (r_5)_j,\end{aligned} \tag{43}$$

$$\begin{aligned}&(\eta_1)_j(\delta Ov_1)_j + (\eta_2)_j(\delta Ov_1)_{j-1} + (\eta_3)_j(\delta Ov_2)_j\\&\quad + (\eta_4)_j(\delta Ov_2)_{j-1} + (\eta_5)_j(\delta Vk_3)_j + (\eta_6)_j(\delta Vk_3)_{j-1}\\&\quad + (\eta_7)_j(\delta Vk_5)_j + (\eta_8)_j(\delta Vk_5)_{j-1} + (\eta_9)_j(\delta Vk_6)_j\\&\quad + (\eta_10)_j(\delta Vk_6)_{j-1} = (r_6)_j,\end{aligned} \tag{44}$$

where

(45)

$$\left.\begin{aligned}
(\eta_1)_j &= \Delta x_j \frac{\Pr\phi_c}{\phi_d}\frac{((Vk_6)_j + (Vk_6)_{j-1})}{4} = (\eta_2)_j,\\
(\eta_3)_j &= -\Delta x_j \frac{\Pr\phi_c}{\phi_d}\frac{((Vk_6)_j + (Vk_6)_{j-1})}{4} = (\eta_4)_j,\\
(\eta_5)_j &= \Delta x_j \frac{Ec\Pr}{\phi_a\phi_d}\frac{((Vk_3)_j + (Vk_3)_{j-1})}{4} = (\eta_6)_j,\\
(\eta_7)_j &= \Delta x_j \frac{\Pr\phi_c}{\phi_d}\frac{((Vk_2)_j + (Vk_2)_{j-1})}{4} = (\eta_8)_j,\\
(\eta_9)_j &= 1 + \frac{N_q\Pr}{\phi_d} + \Delta x_j \frac{\Pr\phi_c}{\phi_d}\frac{((Vk_1)_j + (Vk_1)_{j-1})}{4},\\
(\eta_{10})_j &= -1 - \frac{N_q\Pr}{\phi_d} + \Delta x_j \frac{\Pr\phi_c}{\phi_d}\frac{((Vk_1)_j + (Vk_1)_{j-1})}{4},\\
(r_6)_j &= -((Vk_6)_j - (Vk_6)_{j-1})\\
&\quad - \Pr\frac{Ec}{\phi_a\phi_e}\frac{((Vk_3)_j + (Vk_3)_{j-1})^2}{4}\\
&\quad - \frac{1}{\phi_d}\Pr N_q((Vk_6)_j - (Vk_6)_{j-1})\\
&\quad - \Pr\frac{\phi_d}{\phi_e}MEc\,\sin^2(\Gamma_q)\frac{((Vk_2)_j + (Vk_2)_{j-1})^2}{4}\\
&\quad + \Delta x_j\Pr\frac{\phi_c}{\phi_d}\frac{((Vk_1)_j + (Vk_1)_{j-1})}{2}\frac{((Vk_6)_j + (Vk_6)_{j-1})}{2}\\
&\quad + \Delta x_j\Pr\frac{\phi_c}{\phi_d}\frac{((Vk_2)_j + (Vk_2)_{j-1})}{2}\frac{((Vk_5)_j + (Vk_5)_{j-1})}{2},
\end{aligned}\right\}. \tag{46}$$

5.4 Block tridiagonal structure

The block tridiagonal structure obtained from a linearised set of equations is expressed as follows:

$$A\,\Delta = S, \tag{47}$$

where

$$A = \begin{bmatrix} [L_1] & [N_1] & & & & \\ & [L_2] & [N_2] & & & \\ & & \ddots & & & \\ & & \ddots & & & \\ & & \ddots & & & \\ & & [M_{J-1}] & [L_{J-1}] & [N_{J-1}] \\ & & & [M_J\,] & [L_J\,] \end{bmatrix},$$

$$\Delta = \begin{bmatrix} [\Delta_1] \\ [\Delta_2] \\ \vdots \\ \vdots \\ \vdots \\ [\Delta_{J-1}] \\ [\Delta_J] \end{bmatrix} \text{ and } S = \begin{bmatrix} [S_1] \\ [S_2] \\ \vdots \\ \vdots \\ \vdots \\ [S_{J-1}] \\ [S_J] \end{bmatrix},$$

where the elements defined in equation (46) are expressed as follows:

$$[L_1] = \begin{bmatrix} 0 & 0 & 0 & 1 & 0 & 0 \\ -0.5\Delta x_1 & 0 & 0 & 0 & 0 & 0 \\ -1 & 0 & -0.5\Delta x_1 & 0 & -0.5\Delta x_1 & 0 \\ 0 & -1 & 0 & 0 & 0 & -0.5\Delta x_1 \\ (\Upsilon_6)_1 & 0 & (\Upsilon_8)_1 & (\Upsilon_1)_1 & (\Upsilon_7)_1 & 0 \\ (\eta_6)_1 & (\eta_8)_1 & 0 & (\eta_1)_1 & 0 & (\eta_9)_1 \end{bmatrix},$$

$$[L_j] = \begin{bmatrix} -0.5\Delta x_j & 0 & 0 & 1 & 0 & 0 \\ -1 & -0.5\Delta x_j & 0 & 0 & 0 & 0 \\ 0 & -1 & 0 & 0 & -0.5\Delta x_j & 0 \\ 0 & 0 & -1 & 0 & 0 & -0.5\Delta x_j \\ (\Upsilon_4)_j & (\Upsilon_6)_j & 0 & (\Upsilon_1)_j & (\Upsilon_7)_j & 0 \\ (\eta_4)_j & (\eta_6)_j & (\eta_8)_j & (\eta_1)_j & 0 & (\eta_9)_j \end{bmatrix}, 2 \le j \le J$$

$$[M_j] = \begin{bmatrix} 0 & 0 & 0 & -1 & 0 & 0 \\ 0 & 0 & 0 & 0 & 0 & 0 \\ 0 & 0 & 0 & 0 & -0.5\Delta x_j & 0 \\ 0 & 0 & 0 & 0 & 0 & -0.5\Delta x_1 \\ 0 & 0 & 0 & (\Upsilon_2)_j & (\Upsilon_8)_j & 0 \\ 0 & 0 & 0 & (\eta_2)_j & 0 & (\eta_1 0)_j \end{bmatrix}, \quad 2 \le j \le J$$

$$[N_j] = \begin{bmatrix} -0.5\Delta x_j & 0 & 0 & 0 & 0 & 0 \\ 1 & -0.5\Delta x_j & 0 & 0 & 0 & 0 \\ 0 & 1 & 0 & 0 & 0 & 0 \\ 0 & 0 & 1 & 0 & 0 & 0 \\ (\Upsilon_3)_j & (\Upsilon_5)_j & 0 & 0 & 0 & 0 \\ (\eta_3)_j & (\eta_5)_j & (\eta_7)_j & 0 & 0 & 0 \end{bmatrix}, 1 \le j \le J-1.$$

Now we factorize A as follows:

$$A = LU, \tag{48}$$

where

$$L = \begin{bmatrix} [\Gamma_1] & & & & \\ & [\Gamma_2] & & & \\ & & \ddots & & \\ & & \ddots & [\Gamma_{J-1}] & \\ & & & [M_J\,] & [\Gamma_J\,] \end{bmatrix},$$

$$U = \begin{bmatrix} [I] & [\alpha_1] & & & \\ & [I] & [\alpha_2] & & \\ & & \ddots & \ddots & \\ & & & [I] & [\alpha_{J-1}] \\ & & & & [I] \end{bmatrix}.$$

Each block of super vectors has 6×6 size, while total block-tridiagonal matrix A has $J \times J$ size and $[I]$, $[\Gamma_i]$ and $[\alpha_i]$ are six-ordered matrices. Implementation of LU decomposition algorithm is done to solve Δ. Considerations are done for $\Delta x_j = 0.01$ mesh size to be suitable regarding mathematical observation, and then, final results are attained having error tolerance of 10^{-6}.

Table 4: The assessment of $-\theta'(0)$ by the discrepancy in Prandtl number, $\phi = 0$, $\phi_h = 0$, $N_q = 0$, $E_c = 0$, $S = 0$, and $B_\gamma \rightarrow \infty$

Pr	Ref. [89]	Ref. [90]	Ref. [91]	Ref. [92]	Ref. [93]	Ref. [94]	Present
0.72	0.8086	0.8086	0.80863135	0.80876122	0.80876181	0.80876181	0.80876181
1.0	1.0	1.0	1.0	1.0	1.0	1.0	1.0
3.0	1.9237	1.9236	1.92368259	1.92357431	1.92357420	1.92357420	1.92357420
7.0	3.0723	3.0722	3.07225021	3.07314679	3.07314651	3.07314651	3.07314651
10	3.7207	3.7006	3.72067390	3.72055436	3.72055429	3.72055429	3.72055429

6 Code validation

Verification is done *via* a comparison of currently obtained results with the previous literature [89–94]. The summary on consistency comparison in the presented studies is presented in Table 4. The accurate results are obtained in the present study.

7 Results and discussion

The numerical computation is tabulated and represented graphically for more accessible analysis. The essence of characteristic physical parameters such as Deborah number χ_1, χ_2, magnetic M, angle inclination Γ_q, nanoparticle volume friction ϕ, velocity slip Λ_q, Biot number B_γ, radiation N_q, viscous dissipation Ec, suction ($S > 0$)/injection ($S < 0$), Reynolds number Re, and Brinkman number B_r are discussed thoroughly. The default values were $\Gamma_q = \pi/8$, $M = 0.2$, $\phi = 0.18$, $\phi_h = 0.18$, $\chi_2 = 0.01$, $\mathrm{Pr} = 7.38$, $N_q = 0.2$, $Ec = 0.2$, $\chi_1 = 0.01$, $B_\gamma = 0.2$, $S = 0.1$, $n = 0.2$, $\mathrm{Re} = 5$, and $B_r = 5$.

7.1 Effect of Deborah number (χ_1) and (χ_2)

The dimensionless Deborah number quantifies that given enough time, even a solid-like material can flow, or a fluid-like substance can behave like a solid when it is deformed quickly enough. Because they flow freely, materials with short relaxation periods decompose under stress very quickly. Hence, it is very crucial to overview the consequence of Deborah's number on the system. Figure 4 displays the impact of the relaxation time to retardation time ratio χ_1 on the velocity profile. Whenever χ_1 is intensified, the relaxation time is diminished along with the retardation time. As a result, nanofluid particles acquire a lot more time to return to equilibrium after being in a disturbed manner. As illustrated in Figure 4, the velocity drops as Deborah's number increases. The effect of Deborah's number on temperature is depicted in Figure 5. It is notable that increment of χ_1 caused the temperature amplified. This phenomenon occurs as a result of the fluid flow being slowed by the resistance provided to it. The different effects can be seen with varying the value of χ_2, which has been displayed in Figure 6. It is assumed that χ_2 helps as if there is no resistance being affected by the fluid flow. Nonetheless, a higher value of Deborah corresponds to a longer retardation time because it is dependent on the retardation time of the χ_2

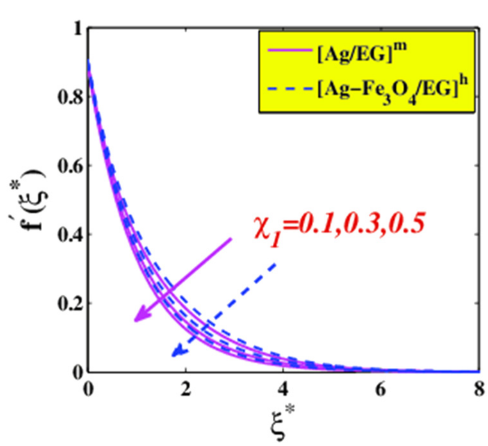

Figure 4: Velocity variation *versus* χ_1.

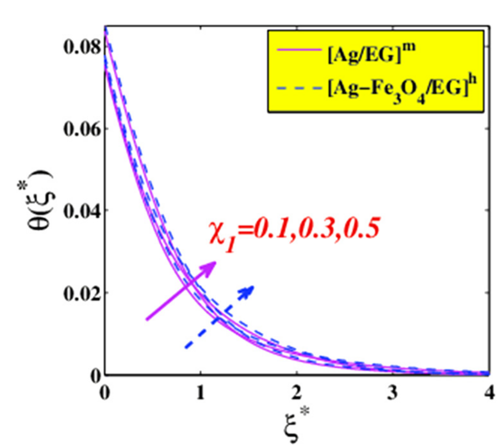

Figure 5: Temperature variation *versus* χ_1.

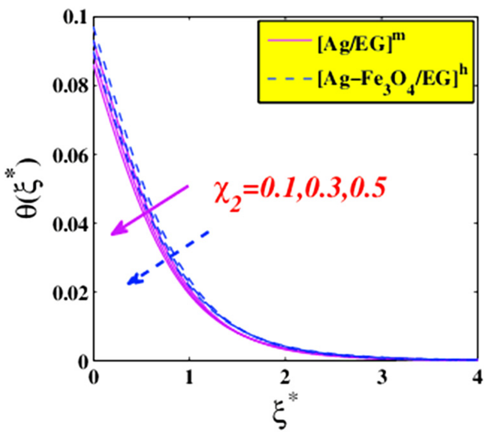

Figure 6: Temperature variation *versus* χ_2.

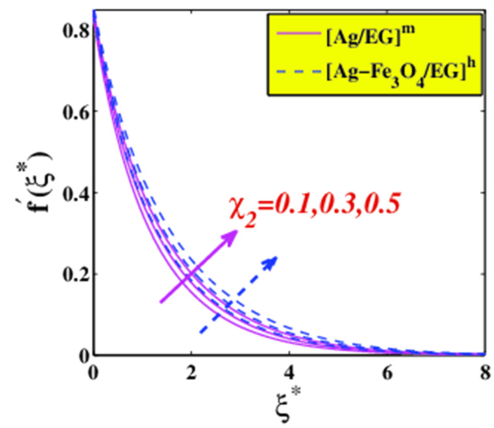

Figure 7: Velocity variation *versus* χ_2.

Table 5: Calculation of Nusselt number Nu $Re_x^{\frac{-1}{2}}$ for Pr = 7.38

S	M	Γ_q	ϕ, ϕ_h	Pr	N_q	B_γ	E_c	Λ_q	χ_1	χ_2	Nu $Re_x^{\frac{-1}{2}}$ Ag-EG	Nu $Re_x^{\frac{-1}{2}}$ Fe_3O_4-Ag/EG	Relative % $\frac{Nu_{(Fe_3O_4-Ag)}-Nu_{(Ag)}}{Nu_{(Fe_3O_4-Ag)}}$
0.1	0.2	$\pi/8$	0.18	7	0.2	0.2	0.2	0.01	0.01	0.01	0.08170	0.10254	20.32%
0.2											0.08218	0.10807	23.95%
0.3											0.08260	0.10919	24.35%
	0.1										0.08116	0.10734	24.38%
	0.5										0.07654	0.10115	24.33%
	1										0.07115	0.09404	24.34%
		$\pi/6$									0.08116	0.10734	24.38%
		$\pi/4$									0.07997	0.10574	24.37%
		$\pi/3$									0.07881	0.10418	24.35%
			0.02								0.10331	0.10945	5.60%
			0.06								0.09139	0.10836	15.66%
			0.1								0.08116	0.10734	24.38%
				10							0.08116	0.10734	24.38%
				15							0.08128	0.10755	24.42%
				20							0.08134	0.10765	24.44%
					0.1						0.07482	0.09897	24.40%
					0.5						0.09968	0.13191	24.43%
					1						0.12934	0.17141	24.54%
						0.1					0.08116	0.10734	24.38%
						0.3					0.22154	0.29251	24.26%
						0.5					0.33870	0.44657	24.15%
							0.2				0.07786	0.10343	24.72%
							0.4				0.07128	0.09560	25.43%
							0.6				0.06469	0.08777	26.29%
								0.1			0.08116	0.10734	24.38%
								0.2			0.08192	0.10819	24.28%
								0.3			0.08230	0.10862	24.23%
									0.1		0.08116	0.10734	24.38%
									0.2		0.08281	0.10932	24.24%
									0.3		0.08370	0.11033	24.13%
										0.1	0.08116	0.10734	24.38%
										0.2	0.08148	0.10774	24.37%
										0.3	0.08175	0.10808	24.36%

as exposed in Figure 7. Technically, elasticity is strengthened by an upsurge in the retardation time of χ_2. Elastic and viscosity effects are observed to be inversely related to one another. Therefore, a diminution in viscosity boosts fluid speed. Thus, the velocity rises as the Deborah number increases. Figures 8 and 9 depict the relationship between χ_1, χ_2 and entropy production in the mono and hybrid nanofluids. It is remarked that χ_2 is highly effective on entropy than χ_1, and both of them reduce the entropy. The hybrid nanofluid is less entropy than the mono as a general. Also, the increasing behaviour of the rate of heat transfer (Table 5) will lead to improving the performance and efficiency of the solar-powered ship.

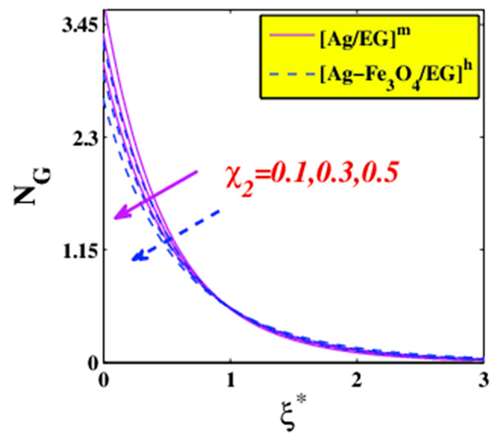

Figure 9: Entropy variation *versus* χ_2.

7.2 Effect of magnetic parameter (M) and angle inclination parameter (Γ_q)

Figure 10 describes the influence of magnetic parameter on velocity distribution. When the magnetic field gets stronger, it creates more drag, which slows down the fluid. Boundary layer flow can be stabilised with the use of a controlled transverse magnetic field. Delaying transition from laminar to turbulent flow can be achieved using this technique. It can be perceived that hybrid nanofluid is slightly improved compared to nanofluid at the same point due to the hybrid nanoparticle in the base fluid, making the fluid challenging to be influenced by the magnetic field. Despite that, the temperature of the system is augmented since less heat can be transferred to other places with the slower movement of the fluid flow. This occurrence is displayed in Figure 11. The positive value indicates that heat is being transported from surface to fluid. It is meaningful to look into the system's entropy with the impact of the magnetic field in the

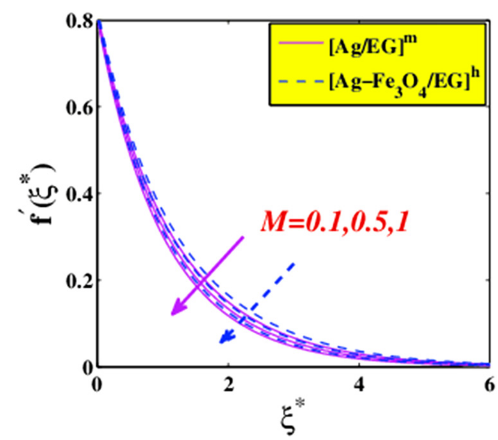

Figure 10: Velocity variation *versus* M.

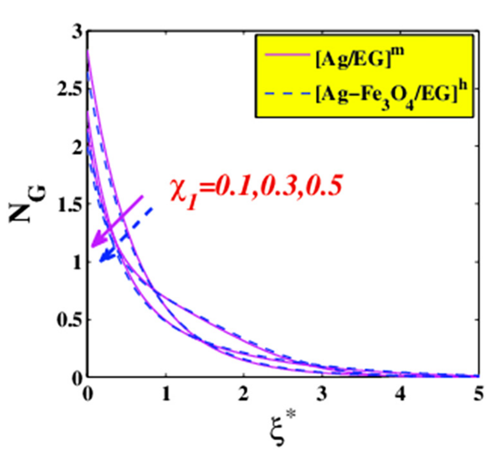

Figure 8: Entropy variation *versus* χ_1.

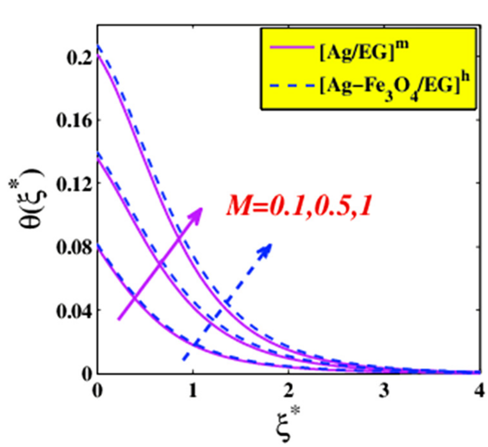

Figure 11: Temperature variation *versus* M.

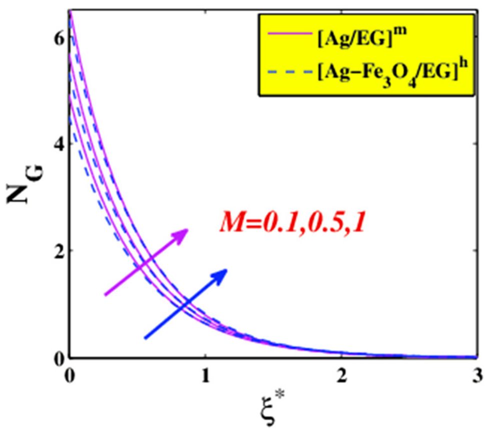

Figure 12: Entropy variation *versus* M.

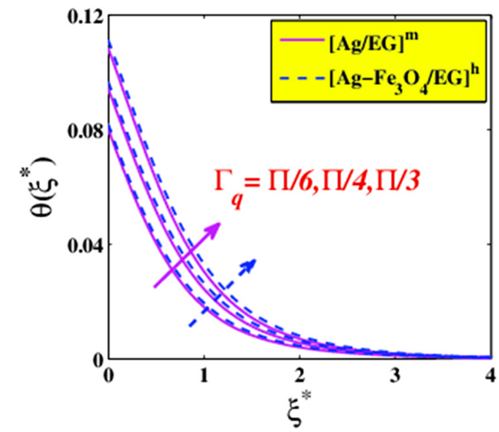

Figure 14: Temperature variation *versus* Γ_q.

system. Figure 12 illustrates the intensified entropy due to the lack of heat transfer in the system. This occurrence is expected due to the diminished velocity, which will retard the heat transportation in the system, hence amplifying the entropy generation in the system.

A similar trend can be found for the influence of angle inclination together with the velocity of the fluid flow demonstrated in Figure 13. The normal force reduces with the increasing inclination angle, which reduces the frictional force. The inclination can be augmented up to the point when the fluid flow begins to slide backward. This action will be the retarded force for the fluid to move forward because of the shift in the normal force. However, the velocity for hybrid nanofluid is slightly better than the conventional nanofluid. The molecule bonding in the base fluid helps the flow to maintain the speed from the retardation force. The temperature system will also intensify due to the slower movement of fluid flow (Figure 14). This phenomenon occurred due to minor heat relocation from the surface towards the flow. The slower movement of the fluid flow causes the buildup of cumulative heat on the surface. Hence, this results in an increment of entropy of the system (Figure 15). It is worth mentioning, regardless of the temperature in the system amplified, that the hybrid nanofluid seems slightly manageable to reduce the entropy generation.

7.3 Effect of nanoparticle volume fraction parameter (ϕ)

Nanoparticle volumetric fraction parameter ϕ effect towards velocity is shown in Figure 16. As ϕ intensified, the speed of the fluid flow is decreased. This occurrence happens due to the increase of fluid viscosity with growing nanofluid concentration and friction escalations. The hybrid nanofluid has a higher velocity than the conventional nanofluid as ϕ augmented. It is found that the temperature of the system

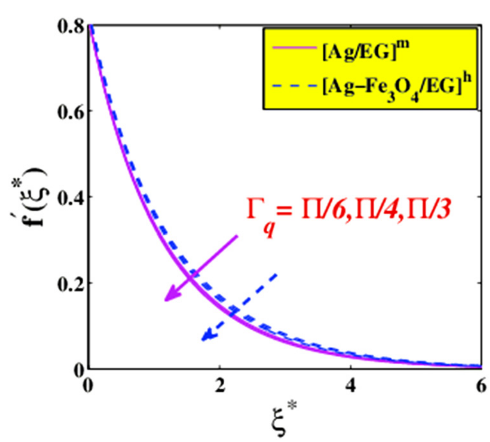

Figure 13: Velocity variation *versus* Γ_q.

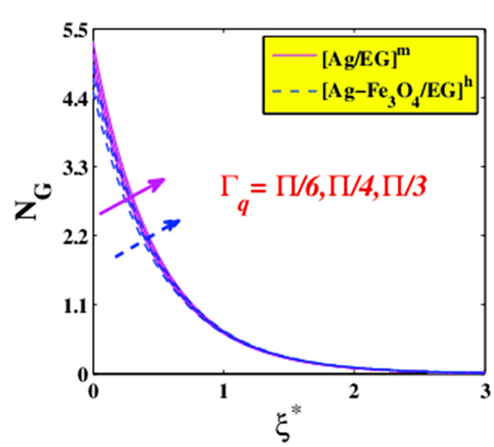

Figure 15: Entropy variation *versus* Γ_q.

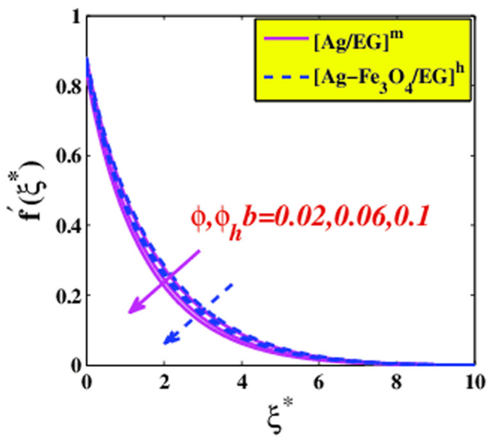

Figure 16: Velocity variation *versus* ϕ.

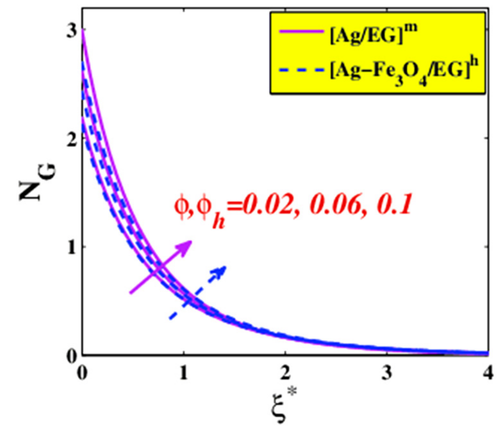

Figure 18: Entropy variation *versus* ϕ.

amplified along with ϕ in Figure 16. It is worth mentioning that fluid velocity is critical for heat transmission. The movement of the particles in the fluid decreased, which will cause the heat to accumulate in the system. Hence, the temperature of the system doubles up. It is also expected that the system's entropy will amplify due to heat accumulation—this evidence is illustrated in Figure 17. The analytical results shown in Figure 18 demonstrate that the nanoparticle volume fraction substantially influences the produced entropy. Conversely, hybrid nanofluid generates less entropy than nanofluid, as shown in Figure 18. This finding implies that hybrid nanofluids can better control the entropy system than nanofluids.

7.4 Effect of velocity slip parameter (Λ_q)

Disparity in velocity between the conveying air and the delivered particles is known as the velocity slip parameter. Along walls, the velocity slip condition is measured. The velocity slip parameter caused the flow velocity to decelerate, as shown in Figure 19. It happens when the slip increases the friction force between the flow and the surface. It is worth pointing out that the velocity of hybrid nanofluid is still higher than nanofluid because the base fluid contains metal particles that have a strong bond that is hard to be affected. Since the velocity is reduced, the temperature of the flow is distending as the velocity slip heightens. This aspect is observable in Figure 20 and obviously happens due to less heat being transported from one point to another. However, it is eye catching that the system's entropy is reduced regardless of the velocity slip intensification, as shown in Figure 21. This phenomenon is because silver and iron have higher positive enthalpies, which have been stated by Hsu *et al.* [95], the bonding energy and structural atoms that are good to be counterbalanced with the entropy.

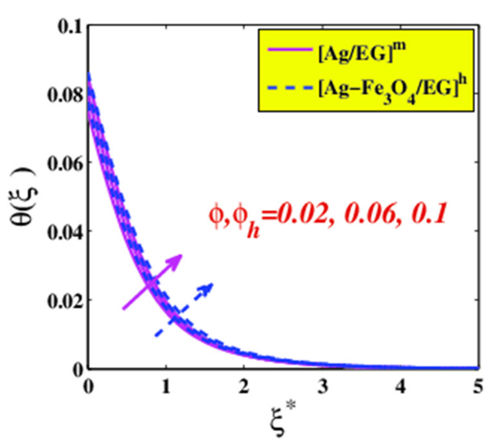

Figure 17: Temperature variation *versus* ϕ.

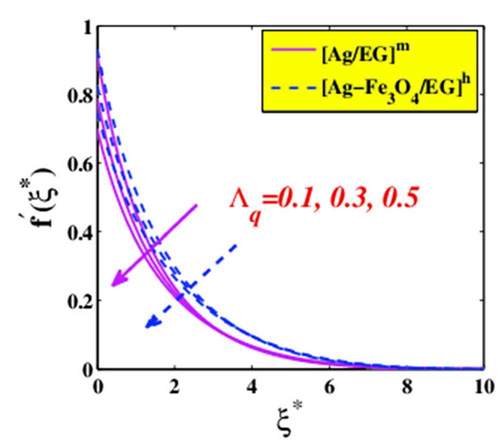

Figure 19: Velocity variation *versus* Λ_q.

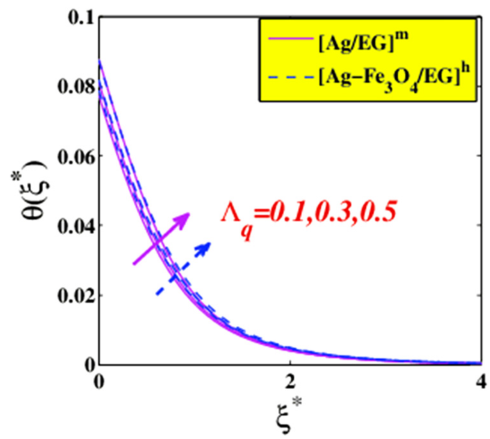

Figure 20: Temperature variation *versus* Λ_q.

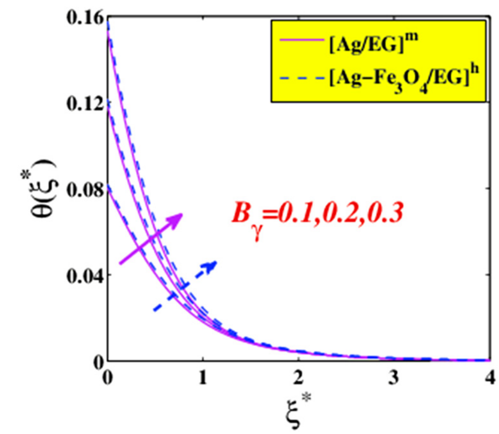

Figure 22: Temperature variations *versus* B_γ.

7.5 Effect of Biot number (B_γ), radiation parameter (N_q), and viscous dissipation (Ec)

The repercussion of the Biot number towards the temperature of the flow is shown in Figure 22. The trend depicted the temperature aggrandize as the Biot number surge. This notable trend showed the thermal resistances inside the flow amplified hence proliferating the temperature of the flow. This peculiarity triggers the entropy of the system enhanced as embellished in Figure 23. It is noteworthy that the increase in the Biot number rises the rate of heat transfer and entropy of the system as well. This increasing behaviour of the rate of heat transfer (Table 5) will lead to improving the performance and efficiency of the solar-powered ship. Moreover, it has been pointed out that the minimum relative percentage of (B_γ) is reflecting on point 24.15 and maximum on point 24.38.

The radiation response resulting from the heat exchange between the flow and surrounding (far field) is displayed in

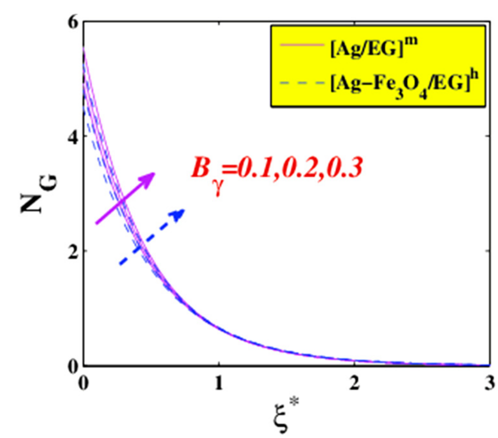

Figure 23: Entropy variations *versus* B_γ.

Figure 24. According to this figure, the surrounding temperature affected the flow temperature to be amplified. This experience is due to both the surrounding and the flow trying to achieve thermal equilibrium with each other. The surrounding temperature is hotter than the flow. Hence, the

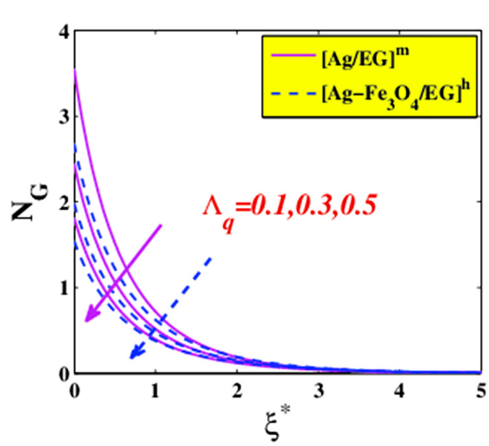

Figure 21: Entropy variation *versus* Λ_q.

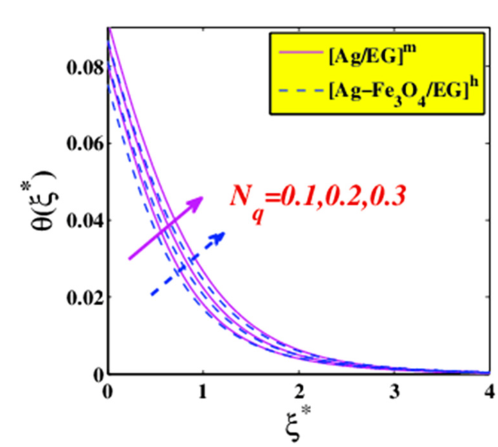

Figure 24: Temperature variations *versus* N_q.

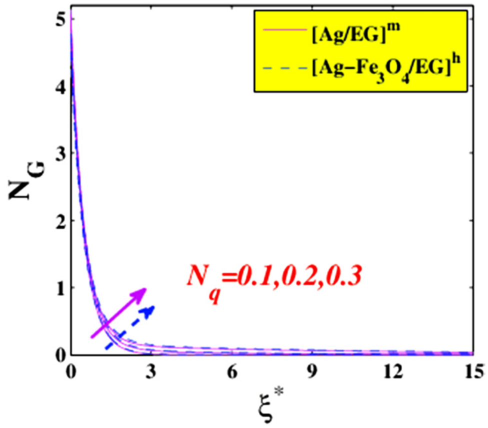

Figure 25: Entropy variations *versus* N_q.

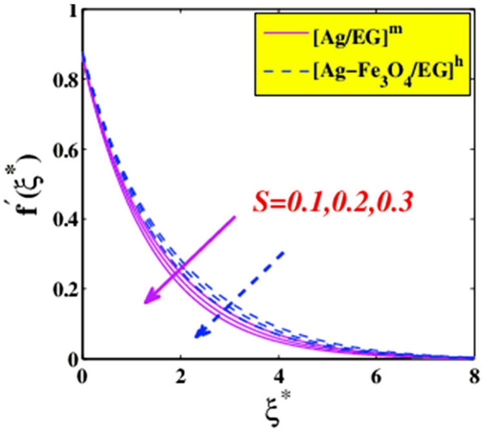

Figure 27: Velocity variations *versus* $S > 0$.

temperature of the flow is elucidated. This incident shows the increment of entropy in the system as illuminated in Figure 25. It embossed that energy in the system undergoes the irreversible process. Also, the increasing behaviour of the rate of heat transfer in Table 5 will lead to improving the performance and efficiency of the solar-powered ship.

A similar trend is shown in Figure 26 as the viscous dissipation exaggerates and the flow's temperature increases. It is widely known that all the energy lost by the viscous dissipation will be converted into heat in the system. Therefore, the total heat in the system increased, and later, the temperature in the flow broadened.

7.6 Effect of suction ($S > 0$)/injection ($S < 0$) parameter

It is essential to look at the essence of the suction or injection parameter towards the flow. Figure 27 shows that the velocity of the flow is diminished as the suction is enhanced. The suction effect will disturb the speed to flow on the surface smoothly. Hence, it will gradually degenerate the velocity of the flow. Nonetheless, the suction effect is an assertion in reducing the temperature of the flow as illustrated in Figure 28. The speed of the nearest layer to the surface increases due to the porosity of the surface. The porosity will pull the flow into the hole. With this effect, the heat can be transmitted quickly, hence reducing the flow's temperature faster. However, the drawback of this outcome is the entropy of the system amplified. The existence of the porosity on the surface makes the entropy a bit hard to control. Thus, the entropy of the system augments, as shown in Figure 29.

Different purport can be seen for the significance of injection parameter towards the fluid flow. Figure 30 shows the enhancement of velocity of a fluid with an escalation of injection parameter. This outcome happens due of the flow is being injected or boosted up to an inner layer, which causes the whole velocity of the flow to be

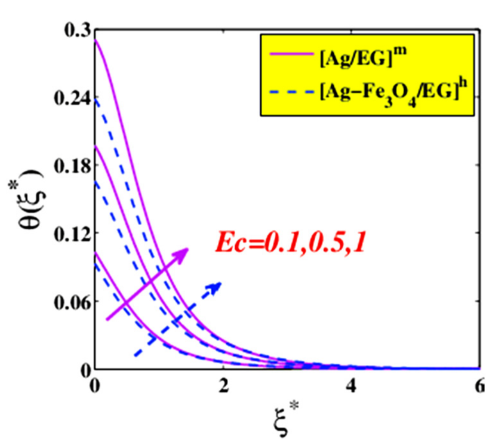

Figure 26: Temperature variations *versus* E_c.

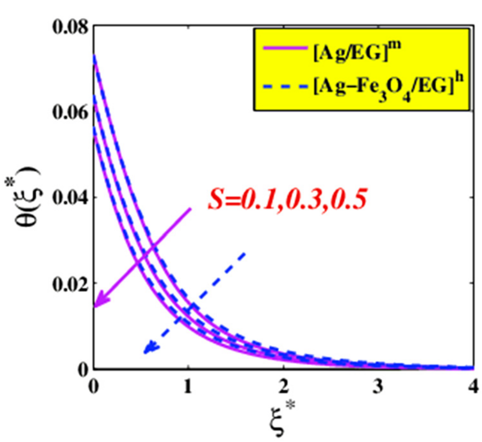

Figure 28: Temperature variations *versus* $S > 0$.

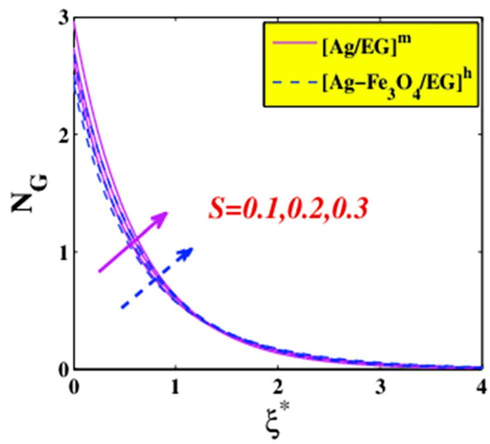

Figure 29: Entropy generation variations *versus* $S > 0$.

augmented. However, the injection parameter side effect adds more friction on the surface, which will cause the temperature of the flow to intensify. This result is apparent in Figure 31. This figure shows that the injection parameter amplified the temperature of the flow. Despite this increment, the entropy of the system is depreciating due to there is no porosity on the surface, which is easier for the system to control the energy in the flow. This circumstance is shown in Figure 32.

7.7 Impact of Reynolds number (Re) and Brinkman number (B_r) on entropy generation

Figure 33 shows that the system's entropy amplifies with the Reynold number because the inertial forces augment the systems. The particles in the hybrid nanofluid have tremendous kinetic energy, which causes them to move faster and have the disorder at a high Reynold number.

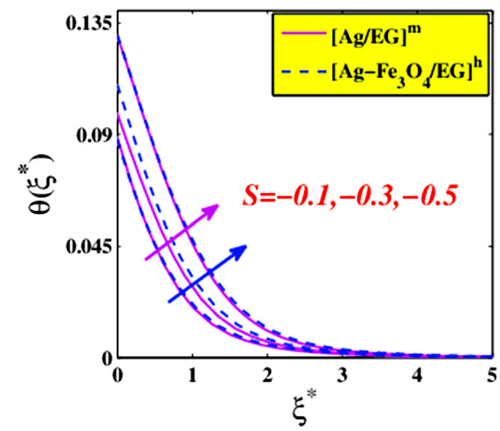

Figure 31: Temperature variations *versus* $S < 0$.

The analysis of the effect of the Brinkman number is eye catching in that it shows the ratio between heat produced by viscous dissipation and heat transmission by molecular conduction. Figure 34 indicates that the Brinkman number expend entropy generation of the system. It is specified that heat produced is more caused by viscous dissipation.

7.8 Impact of (ϕ),(M),(N_q) and (Ec) on heat transfer rate ($Nu_x\ Re_x^{-\frac{1}{2}}$)

It is worth seeing the influence of several factors of the physical parameter that can give impact towards the physical quantity, as such the local Nusselt number. The nanoparticle volume fraction parameter decreases a little heat transfer rate due to the small-sized molecules allowing for free movement and hence micro convection, which can slightly affect the heat transfer. Based on Figure 35, the

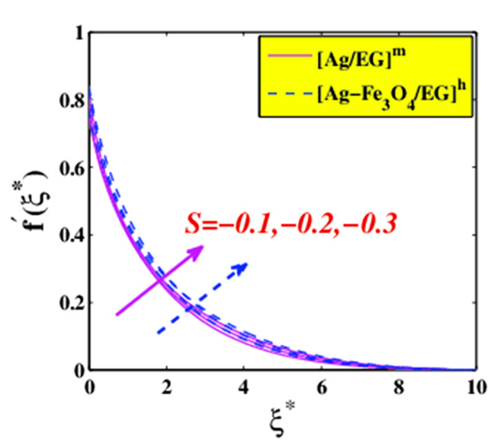

Figure 30: Velocity variations *versus* $S < 0$.

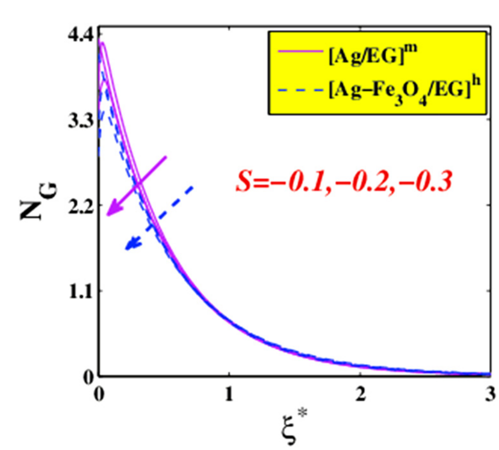

Figure 32: Entropy generation variations *versus* $S < 0$.

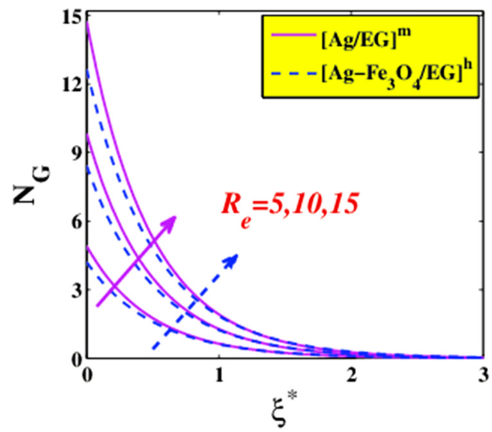

Figure 33: Entropy variations *versus* R_e.

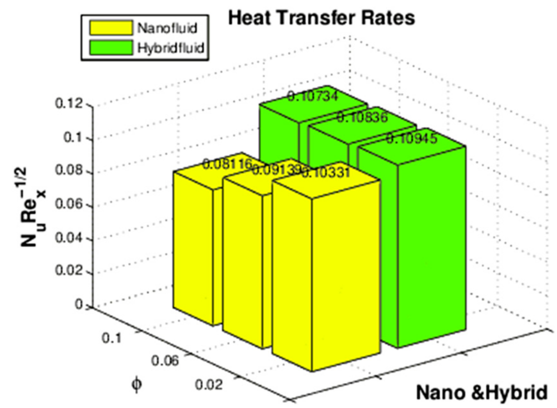

Figure 35: Impact of ϕ on $Nu_x\, Re_x^{-\frac{1}{2}}$.

hybrid nanofluid has at least 5.6% better heat dispersion rather than the nanofluid. This occurrence is due to the hybrid nanofluid advanced properties of thermodynamics. When nanoparticle volume fraction increases, the heat transfer rate for nanofluid decreases significantly compared to hybrid nanofluid. This phenomenon indicates that hybrid nanofluid can maintain heat transfer rates as the volume of nanoparticles augment.

The demeanour of the heat transfer rate with magnetic parameter effect is depicted in Figure 36. The magnetic field acting on the system amplifies as the heat transfer rate reduces in the flow. The flowing current seems like a retarded force in transferring the heat from the surface to the flow. Heat transfer for hybrid nanofluid is more remarkable, at least at 24% than nanofluid. It is due to the base fluid having more metal particles that can uphold the thermal conductivity of the flow.

Figure 37 illustrates that the radiation parameter aggrandizes the heat transfer rate. It is well known that

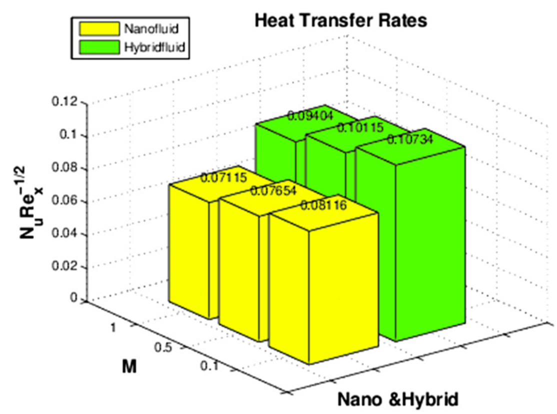

Figure 36: Impact of M on $Nu_x\, Re_x^{-\frac{1}{2}}$.

radiation is the quickest medium in heat transfer because they emit from a body to the receiver flow in electromagnetic waves. With the bits of help of the magnetic parameter, the radiation further heightens the heat transfer rate in the system. It is observable that hybrid nanofluid

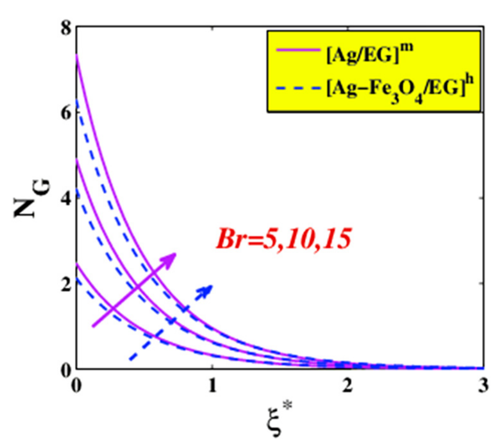

Figure 34: Entropy variations *versus* B_r.

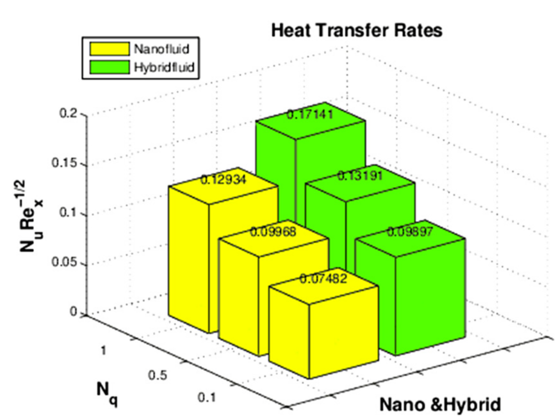

Figure 37: Impact of N_q on $Nu_x\, Re_x^{-\frac{1}{2}}$.

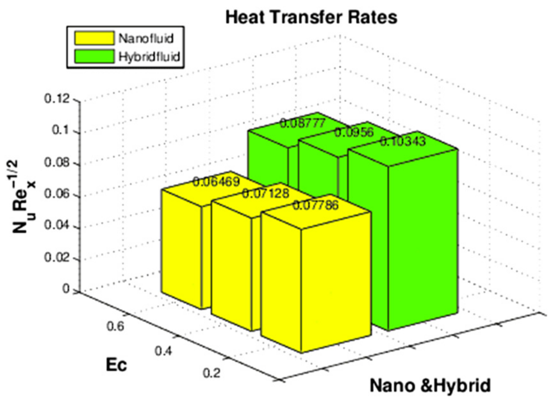

Figure 38: Impact of Ec on $\mathrm{Nu}_x\,\mathrm{Re}_x^{-\frac{1}{2}}$.

possesses better heat transfer, at least about 24% from nanofluid. The physical reason for this phenomenon is that the metal particle in the hybrid nanofluid is more than nanofluid, which can enhance further the heat transfer rate in the system.

The decreasing trend can be observed in Figure 38, which illustrates the depreciation of heat transfer rate with an increment of viscous dissipation. It can be observed that the flow is heating up, but the viscosity of the fluid is low, which is challenging to transform kinetic energy into internal energy of the liquid. However, the hybrid nanofluid has a higher heat transfer rate at about 24% because the viscosity of a fluid is more elevated than the nanofluid.

7.9 Relative heat transfer rate in (Cu–Ag) and ((Fe_3O_4)-EO) nanofluid

It is worth mentioning that the relative percentage for the heat transfer rate of hybrid nanofluid for each physical parameter is 24%. This relative percentage is presented in Table 5. It is seen that almost every physical parameter augment produced an increment at most 24%.

8 Final outcomes

The performance of solar-powered ships using Oldroyd hybrid nanofluids in parabolic trough solar collectors is investigated theoretically. Governing equations involved are altered into ODEs and were further numerically solved using the Keller Box method. All results are analyzed and discussed thoroughly. The results can be summarised as follows:

- Only Deborah number χ_2 and injection parameters amplify velocity of the flow, while Deborah number χ_1, magnetic, angle inclination, nanoparticle volume fraction, velocity slip, and suction parameters diminish the velocity of the flow.
- The temperature profile can be augmented with the influence of Deborah number χ_1, magnetic, angle inclination, nanoparticle volume fraction, velocity slip, radiation, and injection parameter.
- The entropy generation can be controlled by Deborah number, velocity slip, and injection parameter.
- Heat transmission is reduced with the effect of nanoparticle volume fraction, magnetic and viscous dissipation
- Relative percentage of heat transfer rate for hybrid nanofluid is 24% over nanofluid.

8.1 Future direction

The future investigation can include other physical parameters such as Joule heating, nanoparticles shape, and others. The analysis of these factors is critical to have a total overview of solar-powered ships.

Acknowledgments: This work was supported by Taif University researchers supporting project number (TURSP-2020/205), Taif University, Taif, Saudi Arabia.

Funding information: This work was supported by Taif University researchers supporting project number (TURSP-2020/205), Taif University, Taif, Saudi Arabia.

Author contributions: All authors have accepted responsibility for the entire content of this article and approved its submission.

Conflict of interest: The authors state no conflict of interest.

References

[1] Mekhilef S, Faramarzi SZ, Saidur R, Salam Z. The application of solar technologies for sustainable development of agricultural sector. Renew Sustain Energy Rev. 2013;18:583–94.
[2] Bahnemann D. Photocatalytic water treatment: solar energy applications. Sol Energy. 2004;77(5):445–59.
[3] Zhou H, Xu J, Liu X, Zhang H, Wang D, Chen Z, et al. Bio-inspired photonic materials: prototypes and structural effect designs for applications in solar energy manipulation. Adv Funct Mater. 2018;28(24):1705309.
[4] Hassanien RHE, Li M, Lin WD. Advanced applications of solar energy in agricultural greenhouses. Renew Sustain Energy Rev. 2016;54:989–1001.

[5] Hasnain SM, Alawaji SH, Elani UA. Solar energy education-a viable pathway for sustainable development. Renew Energy. 1998;14(1–4):387–92.
[6] Gueymard CA. The sun's total and spectral irradiance for solar energy applications and solar radiation models. Sol Energy. 2004;76(4):423–53.
[7] Ahmed A, Baig H, Sundaram S, Mallick TK. Use of nanofluids in solar PV/thermal systems. Int J Photoenergy. 2019;2019:8039129.
[8] Khanafer K, Vafai K. A review on the applications of nanofluids in solar energy field. Renew Energy. 2018;123:398–406.
[9] Lee Y, Jeong H, Park JT, Delgado A, Kim S. Experimental investigation on evaluation of thermal performance of solar heating system using Al_2O_3nanofluid. Appl Sci. 2020;10(16):5521.
[10] Olia H, Torabi M, Bahiraei M, Ahmadi MH, Goodarzi M, Safaei MR. Application of nanofluids in thermal performance enhancement of parabolic trough solar collector: state-of-the-art. Appl Sci. 2019;9(3):463.
[11] Vijayan G, Rajasekaran K. Performance evaluation of nanofluid on parabolic trough solar collector. Therm Sci. 2020;24(2 Part A):853–64.
[12] Wole-Osho I, Okonkwo EC, Abbasoglu S, Kavaz D. Nanofluids in solar thermal collectors: review and limitations. Int J Thermophys. 2020;4111:1–74.
[13] Jamshed W, Şirin C, Selimefendigil F, Shamshuddin M, Altowairqi Y, Eid MR. Thermal characterization of coolant Maxwell type nanofluid flowing in parabolic trough solar collector (PTSC) used inside solar powered ship application. Coatings. 2021;11(12):1552.
[14] Bayones FS, Jamshed W, Elhag S, Eid MR. Computational Galerkin finite element method for thermal hydrogen energy utilization of first grade viscoelastic hybrid nanofluid flowing inside PTSC in solar powered ship applications. Energy Env. 2022;0958305X221081463. doi: 10.1177/0958305X221081463.
[15] Yang L, Ji W, Mao M, Huang JN. An updated review on the properties, fabrication and application of hybrid-nanofluids along with their environmental effects. J Clean Prod. 2020;257:120408.
[16] Shah TR, Ali MH. Applications of hybrid nanofluids in solar energy, practical limitations and challenges: a critical review. Sol Energy. 2019;183:173–203.
[17] Waini I, Ishak A, Pop I. Unsteady flow and heat transfer past a stretching/shrinking sheet in a hybrid nanofluid. Int J Heat Mass Transf. 2019;136:288–97.
[18] Huang D, Wu Z, Sunden B. Effects of hybrid nanofluid mixture in plate heat exchangers. Exp Therm Fluid Sci. 2016;72:190–6.
[19] Acharya N. On the flow patterns and thermal behaviour of hybrid nanofluid flow inside a microchannel in presence of radiative solar energy. J Therm Anal Calorim. 2020;141(4):1425–42.
[20] Kumar KG, Hani EHB, Assad MEH, Rahimi-Gorji M, Nadeem S. A novel approach for investigation of heat transfer enhancement with ferromagnetic hybrid nanofluid by considering solar radiation. Microsyst Technol. 2021;27(1):97–104.
[21] Ekiciler R, Arslan K, Turgut O, Kurşun B. Effect of hybrid nanofluid on heat transfer performance of parabolic trough solar collector receiver. J Therm Anal Calorim. 2021;143(2):1637–54.
[22] Alzahrani AK, Ullah MZ, Alshomrani AS, Gul T. Hybrid nanofluid flow in a Darcy-Forchheimer permeable medium over a flat plate due to solar radiation. Case Stud Therm Eng. 2021;26:100955.
[23] Chen SB, Jahanshahi H, Abba OA, Solís-Pérez JE, Bekiros S, Gómez-Aguilar JF, et al. The effect of market confidence on a financial system from the perspective of fractional calculus: Numerical investigation and circuit realization. Chaos Solitons Fractals. 2020;140:110223.
[24] Qiang X, Mahboob A, Chu YM. Numerical Approximation of fractional-order volterra integrodifferential equation. J Funct Spaces. 2020;2020:8875792.
[25] Nazeer M, Hussain F, Khan MI, Rehman AU, El- Zahar ER, Chu YM, et al. Theoretical study of MHD electro-osmotically ow of third-grade fluid in micro channel. Appl Math Comput. 2022;420:126868.
[26] Chu YM, Shankaralingappa BM, Gireesha BJ, Alzahrani F, Khan MI, Khan SU. Combined impact of Cattaneo-Christov double diffusion and radiative heat flux on bio-convective flow of Maxwell liquid configured by a stretched nano-material surface. Appl Math Comput. 2022;419:126883.
[27] Zhao TH, Khan MI, Chu YM. Artificial neural networking (ANN) analysis for heat and entropy generation in flow of non-Newtonian fluid between two rotating disks. Math Methods Appl Sci. 2021. doi: 10.1002/mma.7310.
[28] Chu YM, Khan U, Zaib A, Shah SHAM. Numerical and computer simulations of cross-flow in the streamwise direction through a moving surface comprising the significant impacts of viscous dissipation and magnetic fields: stability analysis and dual solutions. Math Probl Eng. 2020;2020:8542396.
[29] Abd El Salam MA, Ramadan MA, Nassar MA, Agarwal P, Chu YM. Matrix computational collocation approach based on rational Chebyshev functions for nonlinear differential equations. Adv Diff Equ. 2021;1:1–17.
[30] Chu YM, Shah NA, Agarwal P, Chung JD. Analysis of fractional multi-dimensional Navier–Stokes equation. Adv Diff Equ. 2021;1:1–18.
[31] Chu YM, Nazir U, Sohail M, Selim MM, Lee JR. Enhancement in thermal energy and solute particles using hybrid nanoparticles by engaging activation energy and chemical reaction over a parabolic surface via finite element approach. Fractal Fract. 2021;5(3):119.
[32] Asjad MI, Zahid M, Chu YM, Baleanu D. Prabhakar fractional-derivative and its applications in the transport phenomena containing nanoparticles. Therm Sci. 2021;25(2):411–6.
[33] Hashim HM, Chu YM. Numerical simulation for heat and mass transport analysis for magnetic-nanofluids flow through stretchable convergent/divergent channels. Int J Mod Phys B. 2021;35(19):2150198.
[34] Asjad MI, Ali R, Iqbal A, Muhammad T, Chu YM. Application of water based drilling clay-nanoparticles in heat transfer of fractional Maxwell fluid over an infinite flat surface. Sci Rep. 2021;11(1):1–14.
[35] Ikram MD, Imran MA, Chu YM, Akgül A. MHD flow of a Newtonian fluid in symmetric channel with ABC fractional model containing hybrid nanoparticles. Comb Chem High Throughput Screen. in press. doi: 10.2174/1386207324666210412122544
[36] Azeem Khan W, Khan M, Malik R. Three-dimensional flow of an Oldroyd-B nanofluid towards stretching surface with heat generation/absorption. PLoS One. 2014;9(8):e105107.

[37] Hafeez A, Khan M, Ahmed J. Flow of magnetized Oldroyd-B nanofluid over a rotating disk. Appl Nanosci. 2020;10(12):5135–47.
[38] Hafeez A, Khan M, Ahmed J. Stagnation point flow of radiative Oldroyd-B nanofluid over a rotating disk. Comput Methods Prog Biomed. 2020;191:105342.
[39] Zhang Y, Zhang M, Bai Y. Flow and heat transfer of an Oldroyd-B nanofluid thin film over an unsteady stretching sheet. J Mol Liq. 2016;220:665–70.
[40] Shivakumara IS, Dhananjaya M, Ng CO. Thermal convective instability in an Oldroyd-B nanofluid saturated porous layer. Int J Heat Mass Transf. 2015;84:167–77.
[41] Ahmad I, Khurshid I, Faisal M, Javed T, Abbas Z. Mixed convective flow of an Oldroyd-B nanofluid impinging over an unsteady bidirectional stretching surface with the significances of double stratification and chemical reaction. SN Appl Sci. 2020;2(9):1–14.
[42] Saqib M, Khan I, Chu YM, Qushairi A, Shafie S, Nisar KS. Multiple fractional solutions for magnetic bio-nanofluid using Oldroyd-B model in a porous medium with ramped wall heating and variable velocity. Appl Sci. 2020;10(11):3886.
[43] Abro KA, Atangana A. A computational technique for thermal analysis in coaxial cylinder of one-dimensional flow of fractional Oldroyd-B nanofluid. Int J Ambient Energy. 2021;1–17. doi: 10.1080/01430750.2021.1939157
[44] Abu-Hamdeh NH, Alsulami RA, Rawa MJ, Aljinaidi AA, Alazwari MA, Eltaher MA, et al. A detailed hydrothermal investigation of a helical micro double-tube heat exchanger for a wide range of helix pitch length. Case Stud Therm Eng. 2021;28:101413.
[45] Abu-Libdeh N, Redouane F, Aissa A, Mebarek-Oudina F, Almuhtady A, Jamshed W, et al. Hydrothermal and entropy investigation of Ag/MgO/H_2O hybrid nanofluid natural convection in a novel shape of porous cavity. Appl Sci. 2021;11(4):1722.
[46] Al-Kouz W, Bendrer BA-I, Aissa A, Almuhtady A, Jamshed W, Nisar KS, et al. Galerkin finite element analysis of magneto two-phase nanofluid flowing in double wavy enclosure comprehending an adiabatic rotating cylinder. Sci Rep. 2021;11(1):1–15.
[47] Alazwari MA, Safaei MR. Combination effect of baffle arrangement and hybrid nanofluid on thermal performance of a shell and tube heat exchanger using 3-D homogeneous mixture model. Mathematics. 2021a;9(8):881.
[48] Alazwari MA, Safaei MR. Non-isothermal hydrodynamic characteristics of a nanofluid in a fin-attached rotating tube bundle. Mathematics. 2021b;9(10):1153.
[49] Algarni M, Alazwari MA, Safaei MR. Optimization of nano-additive characteristics to improve the efficiency of a shell and tube thermal energy storage system using a hybrid procedure: DOE, ANN, MCDM, MOO, and CFD modeling. Mathematics. 2021;9(24):3235.
[50] Ali MS, Anwar Z, Mujtaba M, Soudagar MEM, Badruddin IA, Safaei MR, et al. Two-phase frictional pressure drop with pure refrigerants in vertical mini/micro-channels. Case Stud Therm Eng. 2021;23:100824.
[51] Anitha S, Safaei MR, Rajeswari S, Pichumani M. Thermal and energy management prospects of γ-AlOOH hybrid nanofluids for the application of sustainable heat exchanger systems. J Therm Anal Calorim. 1–17. doi: 10.1007/s10973-021-10996-9.
[52] Dadsetani R, Sheikhzade G, Goodarzi M, Zeeshan A, Ellahi R, Safaei MR. Thermal and mechanical design of tangential hybrid microchannel and high-conductivity inserts for cooling of disk-shaped electronic components. J Therm Anal Calorim. 2021;143(3):2125–33.
[53] do Carmo Zidan D, Maia CB, Safaei MR. Performance evaluation of various nanofluids for parabolic trough collectors. Sustain Energy Technol Assess. 2022;50:101865.
[54] Kapur JN, Kesavan HK. Entropy optimization principles and their applications. Entropy and energy dissipation in water resources. Dordrecht: Springer; 1992. p. 3–20.
[55] Ahmadi MH, Ghazvini M, Sadeghzadeh M, Nazari MA, Ghalandari M. Utilization of hybrid nanofluids in solar energy applications: a review. Nano-Struct Nano-Objects. 2019;20:100386.
[56] Vallejo JP, Sani E, Żyła G, Lugo L. Tailored silver/graphene nanoplatelet hybrid nanofluids for solar applications. J Mol Liq. 2019;296:112007.
[57] Rabbi HMF, Sahin AZ. Performance improvement of solar still by using hybrid nanofluids. J Therm Anal Calorim. 2021;143(2):1345–60.
[58] Ebrahimi D, Yousefzadeh S, Akbari OA, Montazerifar F, Rozati SA, Nakhjavani S, et al. Mixed convection heat transfer of a nanofluid in a closed elbow-shaped cavity (CESC). J Therm Anal Calorim. 2021;144(6):2295–316.
[59] Goodarzi M, Tlili I, Moria H, Cardoso E, Alkanhal TA, Anqi AE, et al. Boiling flow of graphene nanoplatelets nano-suspension on a small copper disk. Powder Technol. 2021;377:10–9.
[60] Jamshed W, Eid MR, Aissa A, Mourad A, Nisar KS, Shahzad F, et al. Partial velocity slip effect on working magneto non-Newtonian nanofluids flow in solar collectors subject to change viscosity and thermal conductivity with temperature. PLoS One. 2021;16(11):e0259881.
[61] Khosravi R, Rabiei S, Khaki M, Safaei MR, Goodarzi M. Entropy generation of graphene–platinum hybrid nanofluid flow through a wavy cylindrical microchannel solar receiver by using neural networks. J Therm Anal Calorim. 2021;145:1949.
[62] Koulali A, Abderrahmane A, Jamshed W, Hussain SM, Nisar KS, Abdel-Aty A-H, et al. Comparative study on effects of thermal gradient direction on heat exchange between a pure fluid and a nanofluid: employing finite volume method. Coatings. 2021;11(12):1481.
[63] Maleki H, Safaei MR, Leon AS, Muhammad T, Nguyen TK. Improving shipboard electronics cooling system by optimizing the heat sinks configuration. J Ocean Eng Sci. 2021. doi: 10.1016/j.joes.2021.09.013.
[64] Mazinani I, Sarafraz MM, Ismail Z, Hashim AM, Safaei MR, Wongwises S. Fluid-structure interaction computational analysis and experiments of tsunami bore forces on coastal bridges. Int J Numer Methods Heat Fluid Flow. 2021;31:1373.
[65] Mourad A, Aissa A, Mebarek-Oudina F, Jamshed W, Ahmed W, Ali HM, et al. Galerkin finite element analysis of thermal aspects of Fe3O4-MWCNT/water hybrid nanofluid filled in wavy enclosure with uniform magnetic field effect. Int Commun Heat Mass Transf. 2021;126:105461.
[66] Safaei MR, Elkotb MA, Alsharif AM, Mansir IB, Alamri S, Tirth V, et al. An innovative design of a high strength and low weight sudden micro expansion by considering a nanofluid: Electronic cooling application. Case Stud Therm Eng. 2021;28:101637.

[67] Safaei MR, Tlili I, Gholamalizadeh E, Abbas T, Alkanhal TA, Goodarzi M, et al. Thermal analysis of a binary base fluid in pool boiling system of glycol–water alumina nano-suspension. J Therm Anal Calorim. 2021;143(3):2453–62.
[68] Shahzad F, Jamshed W, Sathyanarayanan SUD, Aissa A, Madheshwaran P, Mourad A. Thermal analysis on Darcy-Forchheimer swirling Casson hybrid nanofluid flow inside parallel plates in parabolic trough solar collector: an application to solar aircraft. Int J Energy Res. 2021;45(15):20812–34.
[69] Shamshuddin M, Abderrahmane A, Koulali A, Eid MR, Shahzad F, Jamshed W. Thermal and solutal performance of Cu/CuO nanoparticles on a non-linear radially stretching surface with heat source/sink and varying chemical reaction effects. Int Commun Heat Mass Transf. 2021;129:105710.
[70] Shoeibi S, Kargarsharifabad H, Rahbar N, Ahmadi G, Safaei MR. Performance evaluation of a solar still using hybrid nanofluid glass cooling-CFD simulation and environmental analysis. Sustain Energy Technol Assess. 2022;49:101728.
[71] Midilli A, Kucuk H. Mathematical modeling of thin layer drying of pistachio by using solar energy. Energy Convers Manag. 2003;44(7):1111–22.
[72] Lewandowsky S, Brown GD, Thomas JL. Traveling economically through memory space: Characterizing output order in memory for serial order. Mem Cognition. 2009;37(2):181–93.
[73] Guo K, Li H, Yu Z. In-situ heavy and extra-heavy oil recovery: a review. Fuel. 2016;185:886–902.
[74] Minea AA. Hybrid nanofluids based on Al_2O_3, TiO_2 and SiO_2: numerical evaluation of different approaches. Int J Heat Mass Transf. 2017;104:852–60.
[75] Mabood F, Bognár G, Shafiq A. Impact of heat generation/absorption of magnetohydrodynamics Oldroyd-B fluid impinging on an inclined stretching sheet with radiation. Sci Rep. 2020;10:17688.
[76] Aziz A, Jamshed W, Aziz T, Bahaidarah HMS, Rehman KU. Entropy analysis of Powell-Eyring hybrid nanofluid including effect of linear thermal radiation and viscous dissipation. J Therm Anal Calorim. 2020;143:1331–43.
[77] Aziz A, Jamshed W, Aziz T. Mathematical model for thermal and entropy analysis of thermal solar collectors by using Maxwell nanofluids with slip conditions, thermal radiation and variable thermal conductivity. Open Phys. 2018;16:123–36.
[78] Reddy NB, Poornima T, Sreenivasulu P. Influence of variable thermal conductivity on MHD boundary layer slip flow of ethylene-glycol based Cu nanofluids over a stretching sheet with convective boundary condition. J Eng Mathematics. 2014;2014:905158.
[79] Maxwell J. A Treatise on electricity and magnetism. 2nd edn. Oxford, UK: Clarendon Press; 1881.
[80] Ali HM. Hybrid nanofluids for convection heat transfer. USA: Academic Press, Elsevier; 2020.
[81] Rahman MRA, Leong KY, Idris AC, Saad MR, Anwar M. Numerical analysis of the forced convective heat transfer on Al_2O_3–Cu/water hybrid nanofluid. Heat Mass Transf. 2017;53(5):1835–42.
[82] Muhammad K, Hayat T, Alsaedi A, Ahmad B. Melting heat transfer in squeezing flow of basefluid (water), nanofluid (CNTs + water) and hybrid nanofluid (CNTs + CuO+ water). J Therm Anal Calorim. 2021;143(2):1157–74.
[83] Muhammad K, Hayat T, Alsaedi A, Ahmad B, Momani S. Mixed convective slip flow of hybrid nanofluid (MWCNTs + Cu + water), nanofluid (MWCNTs + water) and base fluid (water): a comparative investigation. J Therm Anal Calorim. 2021;143(2):1523–36.
[84] Jamshed W, Aziz A. A comparative entropy based analysis of Cu and Fe_3O_4/methanol Powell-Eyring nanofluid in solar thermal collectors subjected to thermal radiation variable thermal conductivity and impact of different nanoparticles shape. Result Phys. 2018;9:195–205.
[85] Jamshed W, Akgül EK, Nisar KS. Keller box study for inclined magnetically driven Casson nanofluid over a stretching sheet: single phase model. PhysicaScripta. 2021;96:065201.
[86] Hayat T, Nadeem S, Khan AU. Rotating flow of Ag-CuO/H_2O hybrid nanofluid with radiation and partial slip boundary effects. Eur Phys J. 2018;E41:75.
[87] Brewster MQ. Thermal radiative transfer and features. New York City, United States: John Wiley and Sons; 1992.
[88] Keller HB. A new difference scheme for parabolic problems. In: Hubbard B, editor. Numerical solutions of partial differential equation 2; 1971. p. 327–50.
[89] Ishak A, Nazar R, Pop I. Mixed convection on the stagnation point flow towards a vertical, continuously stretching sheet. J Heat Transfer-ASME. 2007;129:1087–90.
[90] Ishak A, Nazar R, Pop I. Boundary layer flow and heat transfer over an unsteady stretching vertical surface. Meccanica. 2009;44:369–75.
[91] Abolbashari MH, Freidoonimehr N, Nazari F, Rashidi MM. Entropy analysis for an unsteady MHD flow past a stretching permeable surface in nano-fluid. Powder Technol. 2014;267:256–67.
[92] Das S, Chakraborty S, Jana RN, Makinde OD. Entropy analysis of unsteady magneto-nanofluid flow past accelerating stretching sheet with convective boundary condition. Appl Mathematics Mech. 2015;36(2):1593–610.
[93] Jamshed W. Numerical investigation of MHD impact on Maxwell nanofluid. Int Commun Heat Mass Transf. 2021;120:104973.
[94] Jamshed W, Nisar KS. Computational single phase comparative study of Williamson nanofluid in parabolic trough solar collector via Keller box method. Int J Energy Res. 2021;45(7):10696–718.
[95] Hsu US, Hung UD, Yeh JW, Chen SK, Huang YS, Yang CC. Alloying behavior of iron, gold and silver in AlCoCrCuNi-based equimolar high-entropy alloys. Mater Sci Eng A. 2007;460–461:403–8.